JOURNAL OF GEOPHYSICAL RESEARCH, VOL. 112, C10014, doi:10.1029/2007JC004296, 2007

Click Here for Full Article

Directional distribution of the short wave estimated from HF ocean radars

Yukiharu Hisaki[1]

Received 18 April 2007; revised 30 July 2007; accepted 10 August 2007; published 13 October 2007.

[1] Short-wave directional distributions estimated using HF (high-frequency) radar are compared with model predictions. The short-wave directional distributions are estimated on the basis of HF radar using two- and four-parameter parametric models to describe short-wave directional distributions. The model-predicted short-wave directional distributions are computed using the energy balance equation. The nonlinear interaction source function in the energy balance equation is calculated from both the exact computation and the discrete interaction approximation (DIA). The predicted short-wave directional distributions from the exact computation and the DIA are compared with those estimated using HF radar. The energy balance equation is simplified by neglecting the propagation term, and the validity of the simplification is investigated. It is found that the four-parameter model is more accurate than the two-parameter model to estimate short-wave directional distribution using HF radar. The model-predicted mean short-wave directions with respect to wind directions are correlated with those estimated from the HF radar. The short-wave direction change associated with a sudden wind shift can be reproduced both from the exact computation and the DIA. The predicted second-order moments of short-wave directional distributions are also correlated with those estimated from the HF radar. This result shows that the model can reproduce transient short-wave directional distributions associated with changes of wind direction. The short-wave directional distributions predicted by the exact computation are narrower than those predicted by the DIA and estimated using the HF radar. The simplification of the energy balance equation is not the main source of the short-wave prediction error.

Citation: Hisaki, Y. (2007), Directional distribution of the short wave estimated from HF ocean radars, *J. Geophys. Res.*, *112*, C10014, doi:10.1029/2007JC004296.

1. Introduction

[2] Ocean surface waves are expressed as a superposition of linear waves of differing frequencies and directions in the first-order approximation. Waves are described in terms of wave spectra $F = F(\omega, \theta)$ at radian frequencies ω and wave directions θ (hereinafter, the clockwise direction with respect to the eastward direction is positive). Wave parameters such as wave height and wave period can be obtained from the wave spectrum $F(\omega, \theta)$.

[3] The parameter characterizing wave directional distribution such as the s-parameter (value of s for $\cos^{2s}(\theta/2)$ distribution) or standard deviation (second-order moment) σ_θ of the directional distribution is less paid attention, especially for the short-wave length. The possible reasons for this are as follows: (1) The wave directional spectrum of short-wave length is less important for marine engineering such as ship navigation and marine construction. (2) The wave directional spectral values of short-wave length are much smaller than the spectral peak values, and are often contaminated by noise in in situ observations.

[4] However, the wave directional spectrum of short-wave length is important for active remote sensing such as scatterometer and HF (high-frequency) ocean radar. It is necessary to estimate the wave directional spectrum at higher wave frequencies sufficient to resolve the Bragg wavelength, which is the same order as the radio wavelength, for predicting radio wave scattering from the sea surface and for remote sensing.

[5] The numerical wave model predicts wave spectra. The energy balance equation is integrated numerically with respect to time as a means to predict wave spectra. Wave parameters such as wave heights and periods are obtained from wave spectra $F(\omega, \theta)$. The wave models such as WAM [*WAMDI group*, 1988] are verified by comparing the wave heights and periods obtained from in situ observations [*WAMDI group*, 1988] or from altimetric remote sensing [*Romeiser*, 1993].

[6] The validation of wave models by comparing wave directional distributions with those obtained from other sensors is important. If it is possible to predict the wave directional spectrum of short-wave length by the wave

[1]Department of Physics and Earth Sciences, Faculty of Science, University of the Ryukyus, Okinawa, Japan.

Copyright 2007 by the American Geophysical Union.
0148-0227/07/2007JC004296$09.00

model, we can predict radio wave scattering by modeling sea surface waves.

[7] The wave directional spectrum by the sea truth is estimated from the cross spectra of measured wave characteristics (e.g., wave elevations, pressures, orbital velocities). However, these wave characteristics are contaminated by noise, and the wave directional spectrum estimated from the sea truth is affected by noise, especially at higher frequencies.

[8] One of the sensors for the estimation of a wave spectrum is HF ocean radar. HF ocean radar can estimate the wave directional spectrum [*Hashimoto et al.*, 2003; *Hisaki*, 1996, 2005, 2006; *Lipa and Nyden*, 2005; *Wyatt*, 1990] and ocean currents [*Hisaki et al.*, 2001; *Hisaki and Naruke*, 2003; *Shay et al.*, 1998; *Takeoka et al.*, 1995]. In particular, parameters characterizing wave directional distribution at the Bragg wavelength such as the s-parameter can be easily estimated, because they are obtained from the first-order scattering which is less affected by noise.

[9] The first-order echoes in the Doppler spectrum of HF radar are much larger than the existing noise and less affected by it. We can expect that the directional distributions at the Bragg frequency (0.505 Hz in this case) estimated using HF ocean radar are more accurate than those based on in situ observations, if the model function of the directional distribution is valid. Therefore HF ocean radar is useful to verify the model's prediction of short-wave directional distribution.

[10] The objective of this study is to verify the model-predicted short-wave (wave of Bragg wavelength) directional distributions by comparing those estimated using HF ocean radar. The wave model for predicting wave spectra is described as

$$\frac{DF}{Dt} = S_t = S_{in} + S_{ds} + S_{nl}, \tag{1}$$

where the total derivatives of $F = F(\omega, \theta)$ with respect to time t includes the propagation term, and S_t is the source function. The source function S_t in the wave model is composed of wind input (S_{in}), dissipation (S_{ds}), and nonlinear interaction source functions (S_{nl}). The parameterization of the nonlinear interaction source function is important for predicting wave directional distributions. For example, *Banner and Young* [1994] showed that the bimodal wave directional distribution can be reproduced from the wave model in which the exact computation of the nonlinear interaction source function is adopted. We focus on the comparison between the exact computation and the discrete interaction approximation (DIA [*Hasselmann and Hasselmann*, 1985]) of the nonlinear interaction source function.

[11] However, it is not feasible to calculate (1) for the exact computation of S_{nl} because of the long computation time. Therefore we take another approach: The wave propagation term in (1) is omitted and

$$\frac{\partial F}{\partial t} = S_{in} + S_{ds} + S_{nl} \tag{2}$$

is used to predict wave spectra. The wave propagation term is omitted from both the exact and the DIA calculation. The validity of equation (2) will be investigated from other data.

[12] Section 2 reviews the method to estimate wave directional distribution from first-order echoes. Section 3 describes the wave model. The observation and data description are reported in section 4. The general features of the model and data analysis are presented in section 5. Section 6 describes the comparison of wave parameters. The validity of equation (2) is investigated in section 7. A discussion and conclusions are presented in section 8.

2. Analysis of HF Radar Doppler Spectrum

[13] HF ocean radar radiates HF radio waves on to the sea surface, and Doppler spectra are obtained by analyzing the scattered signals. Figure 1 shows an example of a Doppler spectrum. The first-order radar cross section, which is proportional to the first-order Doppler spectrum is written as

$$\sigma_1(\omega_D) = 2^6 \pi k_0^4 \sum_{m=\pm 1} S(-2m\mathbf{k}_0)\delta(\omega_D - m\omega_B), \tag{3}$$

where m denotes the sign of the Doppler shift, $\mathbf{k}_0$ is the incident radio wavenumber vector, $k_0 = |\mathbf{k}_0|$, ω_D is a radian Doppler frequency, $\omega_B = (2gk_0)^{1/2}$ is a radian Bragg frequency, g is the acceleration of gravity, $S(\mathbf{k}) = F(\omega, \theta)C_g/k$ is the ocean wave spectrum, $\mathbf{k} = (k\cos\theta, k\sin\theta)$ [e.g., *Barrick*, 1972], and $C_g = \partial\omega/\partial k$ is the group velocity.

[14] The integral of the first-order Doppler spectra is denoted by P_- for negative Doppler frequencies and P_+ for positive Doppler frequencies as shown in Figure 1.

[15] The ratio of the first-order peaks r_i for the beam n_b (n_b = 1,.., N_T, where N_T is the total number of beam directions) and the Doppler spectrum number i is written as

$$r_i = \frac{P_+}{P_-} = \frac{S(-2\mathbf{k}_0)}{S(2\mathbf{k}_0)} = \frac{D(\phi(n_b) + \pi)}{D(\phi(n_b))}, \tag{4}$$

where $D(\theta) = D(\omega_B, \theta)$ is the directional distribution at wavenumber $2k_0$ or radian frequency ω_B, and $\phi(n_b)$ is the radar beam direction for the beam n_b. The normalized wave directional distribution is expressed as

$$D(\theta) = \left[\sum_{k=1}^{L} a_k^2 \cos^{2s}\left(\frac{\theta - \beta_k}{2}\right)\right]\left[2\pi^{1/2}\frac{\Gamma(s+1/2)}{\Gamma(s+1)}\sum_{k=1}^{L} a_k^2\right]^{-1}, \tag{5}$$

where Γ is the Gamma function, $L = 1$ denotes the two-parameter model of the wave directional distribution, $L = 2$ denotes the four-parameter model, s is the spread parameter, $a_1 = 1$, a_2^2 ($a_2^2 \le a_1^2$) denotes the (relative) amplitude of the secondary directional distribution peak, and β_1 and β_2 are dominant directions of primary and secondary peaks, respectively. The number of parameters for the bimodal distribution is $N = 2L = 4$.

[16] *Hisaki* [2004] estimated directional distributions for the $\mathrm{sech}^2(\beta(\theta - \beta_k))$ form [e.g., *Donelan et al.*, 1985] instead of equation (5) in the simulation study, where β is the parameter of the directional distribution. The accuracy of the directional distribution for equation (5) is better than that for the $\mathrm{sech}^2(\beta(\theta - \beta_k))$ form, and equation (5) is used as the directional distribution.

[17] The feasibility of using HF ocean radars to identify the bimodal distribution has been investigated [*Hisaki*,

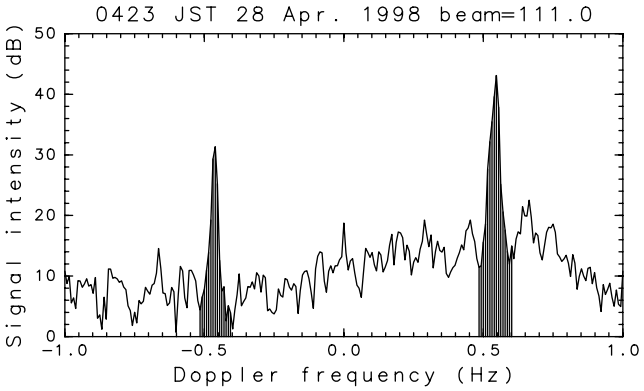

Figure 1. Example of a Doppler spectrum. The shaded areas are P_- and P_+.

2004]. It was shown that the number of beam directions was critical to the accurate estimation of wave parameters in the case of bimodal distribution, and it was strongly suggested that as many radar sites as possible should be used to identify the bimodal distribution [*Hisaki*, 2004]. Therefore the homogeneity of the wave field in the HF radar observation area is assumed in the present study.

[18] If the homogeneity of the wave field is assumed, the wave parameters s, β_k and a_2^2 are estimated by seeking the minima of L_g defined as

$$\log(L_g) = \sum_i^{M_D} \left[-\log(c_i) + \left(1 - \frac{\nu_{1,i}}{2}\right) \log Z_i + \frac{1}{2}(\nu_{1,i} + \nu_{2,i}) \log(\nu_{2,i} + \nu_{1,i} Z_i) + \log\left(\frac{\nu_{1,i}}{\nu_{2,i}} r_{t,i}\right) \right], \tag{6}$$

where

$$\log(c_i) = \frac{\nu_{1,i}}{2} \log \nu_{1,i} + \frac{\nu_{2,i}}{2} \log \nu_{2,i} + \log\left[\Gamma\left(\frac{1}{2}(\nu_{1,i} + \nu_{2,i})\right)\right] - \log\left[\Gamma\left(\frac{\nu_{1,i}}{2}\right)\right] - \log\left[\Gamma\left(\frac{\nu_{2,i}}{2}\right)\right], \tag{7}$$

and M_D is the number of Doppler spectra [e.g., *Hisaki*, 2004; *Wyatt et al.*, 1997]. The value Z_i for Doppler spectrum data number i is

$$Z_i = \frac{\nu_{2,i}}{\nu_{1,i}} \frac{r_i}{r_t(n_b(i))}, \tag{8}$$

and it obeys F-distribution with degrees of freedom ($\nu_{1,i}$, $\nu_{2,i}$), where ($\nu_{1,i}$, $\nu_{2,i}$) is determined on the basis of the signal processing of the Doppler spectra. The value r_i is the observed first-order echo ratio (equation (4)), and $r_t = r_{t,i}$ in equations (6) and (8) is the true Bragg ratio as

$$r_t(n_b(i)) = \frac{D(\phi(n_b) + \pi)}{D(\phi(n_b))} = \left[\sum_{k=1}^{L} a_k^2 \sin^{2s}\left(\frac{\phi(n_b) - \beta_k}{2}\right)\right] \cdot \left[\sum_{k=1}^{L} a_k^2 \cos^{2s}\left(\frac{\phi(n_b) - \beta_k}{2}\right)\right]^{-1}. \tag{9}$$

The area-averaged short-wave parameters are estimated in this method.

[19] Because two radars are used, the wave parameters can be estimated for the two-parameter model ($L = 1$ in equation (5)) in the two-radar coverage area by solving equation (4) [*Hisaki*, 2002]. The ratios of the first-order peaks are spatially interpolated on regular grid points. The wave parameters β_1 and s are estimated on regular grids. The horizontal variability is assessed from gridded β_1 and s. In order to compare radar-estimated wave directional distributions with the model's predictions, second-order moments of wave directional distributions are calculated as

$$\sigma_\theta(\omega) = \left[\int_{\theta_m - \pi}^{\theta_m + \pi} (\theta - \theta_m)^2 D(\omega, \theta) d\theta\right]^{1/2}, \tag{10}$$

where $\theta_m = \theta_m(\omega)$ is the mean direction for the normalized distribution $D(\omega, \theta)$. Equation (10) is used for both radar estimations and model predictions. The value $\sigma_\theta(\omega)$ is a useful measure of wave directional distribution, because it does not require any a priori assumption regarding the shape of the directional distribution.

3. Wave Model

[20] The parameterization of the source function is the same as WAM cycle 3 except for the nonlinear interaction source function. The wind input source function S_{in} is written as

$$S_{in} = \beta F(\omega, \theta), \tag{11}$$

where

$$\Theta = 0.25 \frac{\rho_a}{\rho_w} \left(28 \frac{u_*}{c} \cos(\theta - \theta_w) - 1\right) \omega \tag{12}$$

$$\beta = \max[0, \Theta], \tag{13}$$

where θ is the direction of wavenumber vector $\mathbf{k}$, θ_w is the wind direction, ρ_a (ρ_w) is the air (water) density and $c = \omega/k$ is the phase speed. The friction velocity u_* is written as

$$u_* = C_D^{1/2} u, \tag{14}$$

where the drag coefficient C_D is

$$C_D = c_{d1} + c_{d2} u, \tag{15}$$

$c_{d1} = 0.8 \times 10^{-3}$, $c_{d2} = 0.065 \times 10^{-3}$, u is the wind speed at 10 m height [*Wu*, 1980].

[21] The dissipation source function S_{ds} for deep water is written as

$$S_{ds} = -\alpha_d \hat{\omega} \left(\frac{\omega}{\hat{\omega}}\right)^2 \left(\frac{\hat{\alpha}}{\hat{\alpha}_{PM}}\right)^2 F(\omega, \theta) \tag{16}$$

where

$$\hat{\alpha} = E_0 \hat{\omega}^4, \tag{17}$$

$$E_0 = \int_{-\pi}^{\pi} \int_0^{\infty} F(\omega, \theta) d\omega d\theta, \tag{18}$$

$$\Omega = \int_{-\pi}^{\pi} \int_0^{\infty} F(\omega, \theta) \omega^{-1} d\omega d\theta, \tag{19}$$

$$\hat{\omega} = E\Omega^{-1}, \tag{20}$$

$\hat{\alpha}_{PM} = 3.016 \times 10^{-3}$ and $\alpha_d = 2.33 \times 10^{-5}$ [*WAMDI group*, 1988].

[22] The nonlinear interaction source function S_{nl} is calculated by the exact computation and DIA. The method of exact computation is based on that described by *Komatsu and Masuda* [2001], which is improved from *Masuda* [1980] and *Komatsu et al.* [1993]. The advantage of this method is that the numerical integration of equation (A1) is stable, while the exact NL [*Hasselmann and Hasselmann*, 1981] is unstable owing to the singularities at $S_0 = 0$ in equation (A6). The numerical computation method of S_{nl} in equation (2) by exact computation is described in Appendix A.

[23] The DIA is also used for comparison. In the DIA, two quadruplets of wavenumber vectors $\mathbf{k}_1$, $\mathbf{k}_2$, $\mathbf{k}_{3N}$ and $\mathbf{k}_4$ are considered, both with wave frequencies:

$$\omega_1 = \omega_2 = \omega \tag{21}$$

$$\omega_3 = (1 + \lambda_{nl})\omega = \omega_+ \tag{22}$$

$$\omega_4 = (1 - \lambda_{nl})\omega = \omega_-. \tag{23}$$

The wavenumber vector directions with frequencies ω_1, ω_2, ω_3, and ω_4 are respectively θ_1, θ_2, θ_3, and θ_4, and they are written as

$$\theta_1 = \theta_2 = \theta \tag{24}$$

$$\theta_3 - \theta = \pm\theta_+ = \pm \arccos\left(\frac{1 + 2\lambda_{nl} + 2\lambda_{nl}^3}{(1 + \lambda_{nl})^2}\right) \tag{25}$$

$$\theta_4 - \theta = \mp\theta_- = \mp \arccos\left(\frac{1 - 2\lambda_{nl} - 2\lambda_{nl}^3}{(1 - \lambda_{nl})^2}\right) \tag{26}$$

and $\lambda_{nl} = 0.25$.

[24] The increment of wave energy for deep water is

$$\begin{pmatrix} \delta S_{nl} \\ \delta S_{nl}^{+} \\ \delta S_{nl}^{-} \end{pmatrix} = \begin{pmatrix} 2\Delta\omega\Delta_\theta/\Delta\omega\Delta_\theta \\ (1 + \lambda_{nl})\Delta\omega\Delta_\theta/\Delta\omega_+\Delta_\theta \\ (1 - \lambda_{nl})\Delta\omega\Delta_\theta/\Delta\omega_-\Delta_\theta \end{pmatrix} D_d(\omega, \omega_3, \omega_4, \theta, \theta_3, \theta_4), \tag{27}$$

$$D_d(\omega, \omega_3, \omega_4, \theta, \theta_3, \theta_4) = (2\pi)^{-9} C_0 \omega^{11} \cdot \left[(F(\omega, \theta))^2 \left\{ \frac{F(\omega_3, \theta_3)}{(1 + \lambda_{nl})^4} + \frac{F(\omega_4, \theta_4)}{(1 - \lambda_{nl})^4} \right\} - 2\frac{F(\omega, \theta)F(\omega_3, \theta_3)F(\omega_4, \theta_4)}{\left(1 - \lambda_{nl}^2\right)^4} \right], \tag{28}$$

where δS_{nl}, δS_{nl}^{+}, and δS_{nl}^{-} are increments at wavenumber vectors $\mathbf{k}_1 (= \mathbf{k}_2)$, $\mathbf{k}_3$, and $\mathbf{k}_4$ respectively, and $C_0 = 3 \times 10^7$ [e.g., *Hasselmann et al.*, 1985]. The frequency resolution at ω, ω_+, and ω_- are respectively $\Delta\omega$, $\Delta\omega_+$, and $\Delta\omega_-$. The angular increment Δ_θ is a constant.

4. Observation

4.1. HF Radar Observation

[25] The HF ocean radar of the Okinawa Radio Observatory, Communications Research Laboratory (Okinawa Subtropical Environment Remote-Sensing Center, National Institute of Information and Communications Technology) was deployed along the coast of the eastern part of Okinawa Island. The observation of ocean current fields and surface waves using this HF ocean radar was conducted from 15 April 1998 to 15 May 1998. The radio frequency was 24.5 MHz, the Bragg wavelength 6.1 m, and the radian Bragg frequency $\omega_B = 3.179$ rad/s. The temporal resolution of the radar system was 2 hours.

[26] Figure 2 shows HF radar observation area. The radar stations were located at site A (26°7.19′N, 127°45.78′E) and site B (26°18.63′N, 127°50.25′E). The details of the observation and the radar system have been previously described [*Hisaki et al.*, 2001; *Hisaki*, 2002]. The Doppler spectra are sampled at radial grids with origin at radar positions. The radial resolution is 1.5 km. The area-averaged wave parameters are estimated using radial grids as shown in Figure 2. The homogeneity of the wave field in the radar observation area is assumed. The effect of the assumption on the wave prediction error will be investigated in section 7.

[27] The gridded wave parameters are estimated using first-order Bragg echoes on the grid points shown in Figure 2. The first-order Bragg echoes on the regular grid points are estimated using a bilinear spatial interpolation. The resolution of the regular grid is 1.5 km. The estimated short-wave parameters are only s and β_1 for $L = 1$ in equation (5). These parameters can be used to diagnose the horizontal variabilities of wave fields.

4.2. Other Data

[28] Wind data on the sea surface are not available. The surface wind data at 10-min intervals at station I (Itokazu,

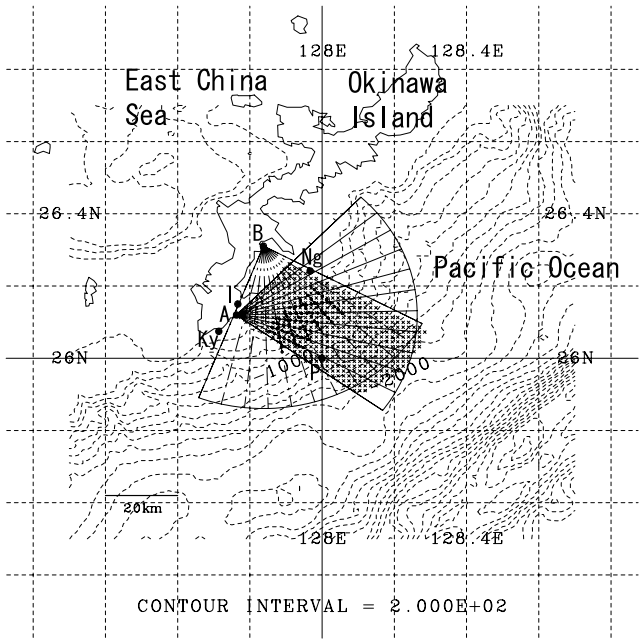

Figure 2. Map of the observation area. A and B, locations of the HF ocean radars; I, meteorological station; Ky and Ng, wave observation points; P, JMA-analyzed wave data point. The black circles are radial grid points sampling Doppler spectra for estimating area-averaged wave parameters, and crosses are regular grid points to estimate gridded wave parameters.

26°09′N, 127°46′E) in Figure 2 were supplied by the Japan Meteorological Agency (JMA). The comparison of wind directions at station I and short-wave directions estimated using HF radar shows the root-mean-square (RMS) difference between them is 31° [*Hisaki*, 2002]. In addition, most of the outliers in the scatter diagram between wind directions at station I and short-wave directions estimated using HF radar are associated with sudden changes of wind direction.

[29] Wave height was observed at station Ky (Kyan, 26°4′N, 127°43′E) in Figure 2 by JMA. An ultrasonic wave height meter was used for measurement at a water depth of 51 m and 1370 m off the coast. The wave sensor measures surface waves at 0.25-s intervals. The hourly significant wave heights and periods were estimated using the zero-up-cross method based on 20 min of observation (4800 samples) of surface displacements.

[30] The wave heights are also observed at station Ng (Nakagusuku, 26°14.5′ 127°58′) in Figure 2 by Port and Harbour Research Institute. The wave sensor measures surface waves at 0.5-s intervals. The significant wave heights and periods were estimated using the zero-up-cross method based on 20 min of observation of surface displacements at 2-hour intervals.

[31] Wave and wind data every 9 Japan Standard Time (JST) at P in Figure 2 (26°N, 128°E) are also available [*Japan Meteorological Agency*, 1999, Figure 5]. The wave heights and directions are hindcasted using the numerical model [*Ichinari and Kohno*, 1997]. The JMA wave model is a WAM-type model, although there are differences in the parameterizations of the source functions.

5. General Features

5.1. Comparison Between Exact Computation and DIA

[32] Figure 3 shows examples of the nonlinear source function $S_{nl}(\omega, \theta)$. The wave spectrum is the JONSWAP type and the Mitsuyasu-Hasselmann distribution [*Mitsuyasu et al.*, 1975; *Hasselmann et al.*, 1980] as

$$F(\omega, \theta) = E(\omega)D(\omega, \theta), \tag{29}$$

where $E(\omega)$ is the frequency spectrum written as

$$E(\omega) = \alpha\omega^{-5} \exp\left(-\frac{5}{4}\frac{\omega^4}{\omega_m^4} \exp\left\{ (\log\gamma) \exp\left[-\frac{(\omega-\omega_m)^2}{2\sigma^2\omega_m^2} \right] \right\} \right) \tag{30}$$

with $\gamma = 3.3$, $\sigma = 0.07$ for $\omega < \omega_m$, $\sigma = 0.09$ for $\omega > \omega_m$, and $\alpha = 8.1 \times 10^{-3}$. The directional distribution is given by equation (5) with $L = 1$, $\beta_1 = 0$ and

$$s = 10^{0.99}(\omega/\omega_m)^{\beta_s}, \tag{31}$$

where $\beta_s = 4.06$ for $\omega < \omega_m$ and $\beta_s = -2.34$ for $\omega \geq \omega_m$. The peak wave frequency is $\omega_m = 0.4\pi$ rad/s. The minimum and maximum radian frequencies are respectively $\omega_{\min} = 0.453$ (rad/s) and $\omega_{\max} = 5.551$ (rad/s), which corresponds to wavelengths of 300 m and 2 m, respectively.

[33] Figures 3a and 3b show integrals of the nonlinear source functions with respect to θ., i.e., $T_1(\omega) = \int S_{nl}(\omega, \theta)d\theta$. The difference between exact computation and the DIA is same as that of *Hasselmann et al.* [1985]. For example, the strong negative lobe appears in the DIA (Figure 3b). The differences of $T_1(\omega)$ between different wave frequency and direction resolutions are not so large in exact computation. The peaks of the $T_1(\omega)$ are more dependent on frequency resolution rather than on direction resolution. This fact shows that the peak wave frequencies of $T_1(\omega)$ are not captured in the coarse wave frequency resolution case. The present method of exact computation of the nonlinear source function is stable.

[34] Figure 4 shows wave spectra calculated from equation (2) for the exact computation of S_{nl} (hereinafter, referred to as ''exact computation'') and the DIA. The wind speed is 7 m/s and the integration time is 7 days. The wave heights ($4E_0^{1/2}$) for exact computation and the DIA are 0.75 m and 0.83 m, respectively. The shapes of the wave frequency spectra are similar to each other. The short-wave directional distribution calculated by exact computation is narrower than that calculated by the DIA.

[35] The directional distributions are bimodal for lower frequencies (i.e., smaller than 1 rad/s in Figures 4b and 4d). This bimodal structure is clearer in Figure 4b (exact computation) than in Figure 4d (DIA). The nonlinear transfer function $S_{nl}(\omega, \theta)$ for a fixed ω lower than 1 rad/s has two peaks which are symmetrical with respect to $\theta = 0°$. The difference between the maximum and the minimum value of $S_{nl}(\omega, \theta)$ for a fixed ω lower than 1 rad/s

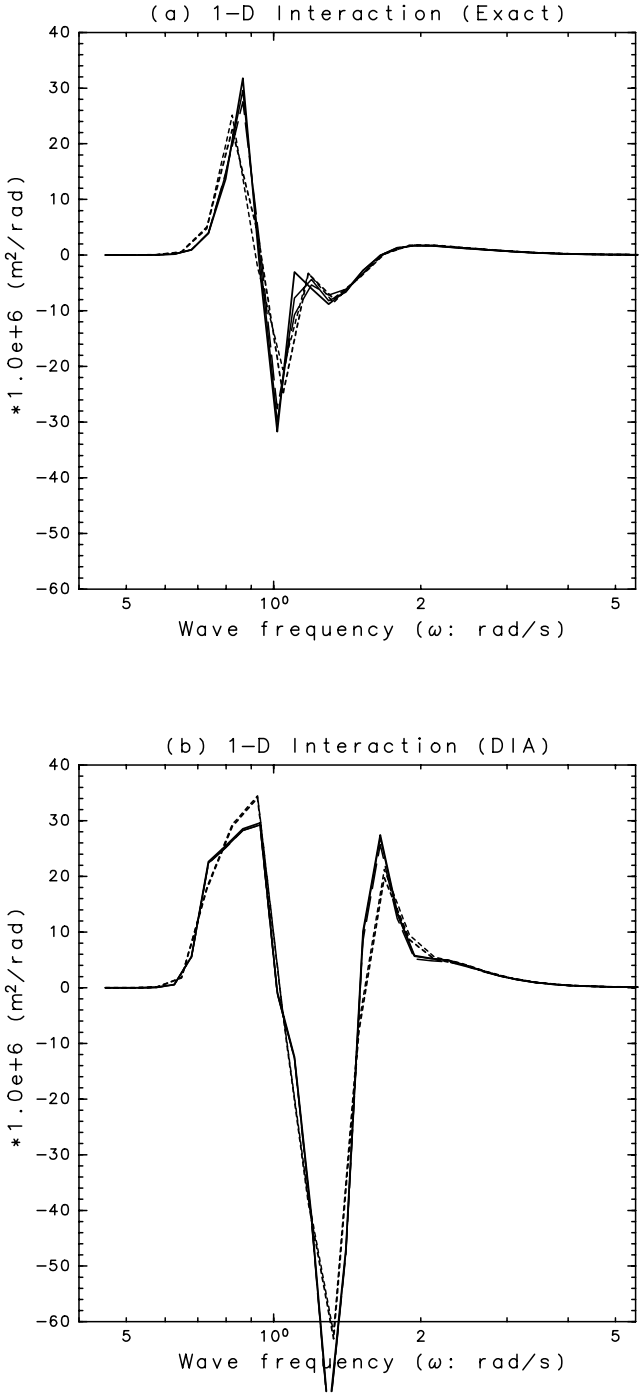

Figure 3. Examples of the nonlinear source function $S_{nl}(\omega, \theta)$. (a) Exact computation of $T_1(\omega)$ (integral of $S_{nl}(\omega, \theta)$ with respect to θ) and (b) DIA of $T_1(\omega)$ for the spectrum as in equations (29), (30), and (31). Thick solid line, $N_{\max} = 32$, $M = 36$; thick dotted line, $N_{\max} = 22$, $M = 20$; thin solid line, $N_{\max} = 32$, $M = 24$; thin dotted line, $N_{\max} = 22$, $M = 36$; thin dashed line, $N_{\max} = 32$, $M = 20$.

calculated by exact computation is larger than that calculated from the DIA. Therefore a bimodal structure for lower frequencies is clear in the case of the exact computation as seen in Figure 4b.

5.2. Wave Model Parameters

[36] The model parameters to predict wave parameters are as follows: The minimum and maximum radian frequencies are respectively $\omega_{\min} = 0.453$ (rad/s) and $\omega_{\max} = 5.551$ (rad/s). The number of frequencies is $N_{\max} = 32$ and the frequency step is $r_\omega = 1.084$ (equation (A17)). The number of directions is $M = 24$ (equation (A18)). The minimum threshold of the kernel in equation (A6) is $K_{\min} = 10^{-6}$ and the number N_{34} (equation (A19)) is $N_{34} = 29$. The sea surface wind data is not available. We calculated wave spectra for winds as

$$\mathbf{u} = a_w(U_I \cos\theta_I, U_I \sin\theta_I), \tag{32}$$

where U_I and θ_I show wind speeds and directions at station I in Figure 2. The directions θ_I agree with HF radar-estimated short-wave directions [*Hisaki*, 2002], thus they are typical values of wind directions on the sea surface. Because we do not know the value of the factor a_w, we calculated for various a_w and investigated the sensitivity of wave parameter predictions on the factor a_w. The integration of equation (2) starts from 00 JST 14 April, 1998. The time step is 240 sec, and the semi-implicit scheme [*WAMDI group*, 1988] is used.

5.3. Wave and Wind Data

[37] Figure 5 shows the time series of wave parameters and winds during the HF radar observation period. The wave heights at Ky (H_k) and Ng (H_n) (Figure 2) agree closely with each other. The difference of wave heights at Ky and Ng is large on 25 April 1998 when the atmospheric front passed near the HF radar observation area [*Hisaki*, 2002]. The difference of wave heights is also large on 3 May 1998 when the atmospheric front is close to the HF radar observation area [*Japan Meteorological Agency*, 1998].

[38] The temporary change of JMA-analyzed wave heights at P in Figure 2 (26°N, 128°E) is similar to that of wave heights at Ky and Ng (Figure 5a). The mean wave heights during the period at Ky, Ng, and P in Figure 2 (26°N, 128°E) are 0.85 m, 0.95 m, and 1.3 m, respectively.

[39] Figure 5b shows the time series of significant wave periods. The wave periods at both Ky and Ng are long on 19 April, 26 April, and 9 May. Some of them are associated with the local maxima of wave heights, but some are not. For example, the wave height and wind speeds are not as large on 19 April, suggesting that the swell is dominant.

[40] Figure 5c shows the time series of hourly wind speeds U_I at the station I and JMA-analyzed wind speeds at P in Figure 2 (26°N, 128°E). The temporary change of JMA-analyzed wind speeds are similar to those of wind speeds recorded at station I. The mean wind speeds at P (26°N, 128°E) and station I are 4.8 and 4.0 m/s, respectively. Figure 5d shows the time series of wave and wind directions at the station I and JMA analyzed wind directions at P in Figure 2 (26°N, 128°E). The fetch is unlimited in most of the period. The RMS difference of wind directions at station I (θ_I) and JMA-analyzed wind directions (θ_W) is 62°, which is larger than the difference between HF radar short-wave directions and wind directions at station I. This is due to the horizontal variability of winds. The difference between wind directions at station I (θ_I) and JMA-analyzed

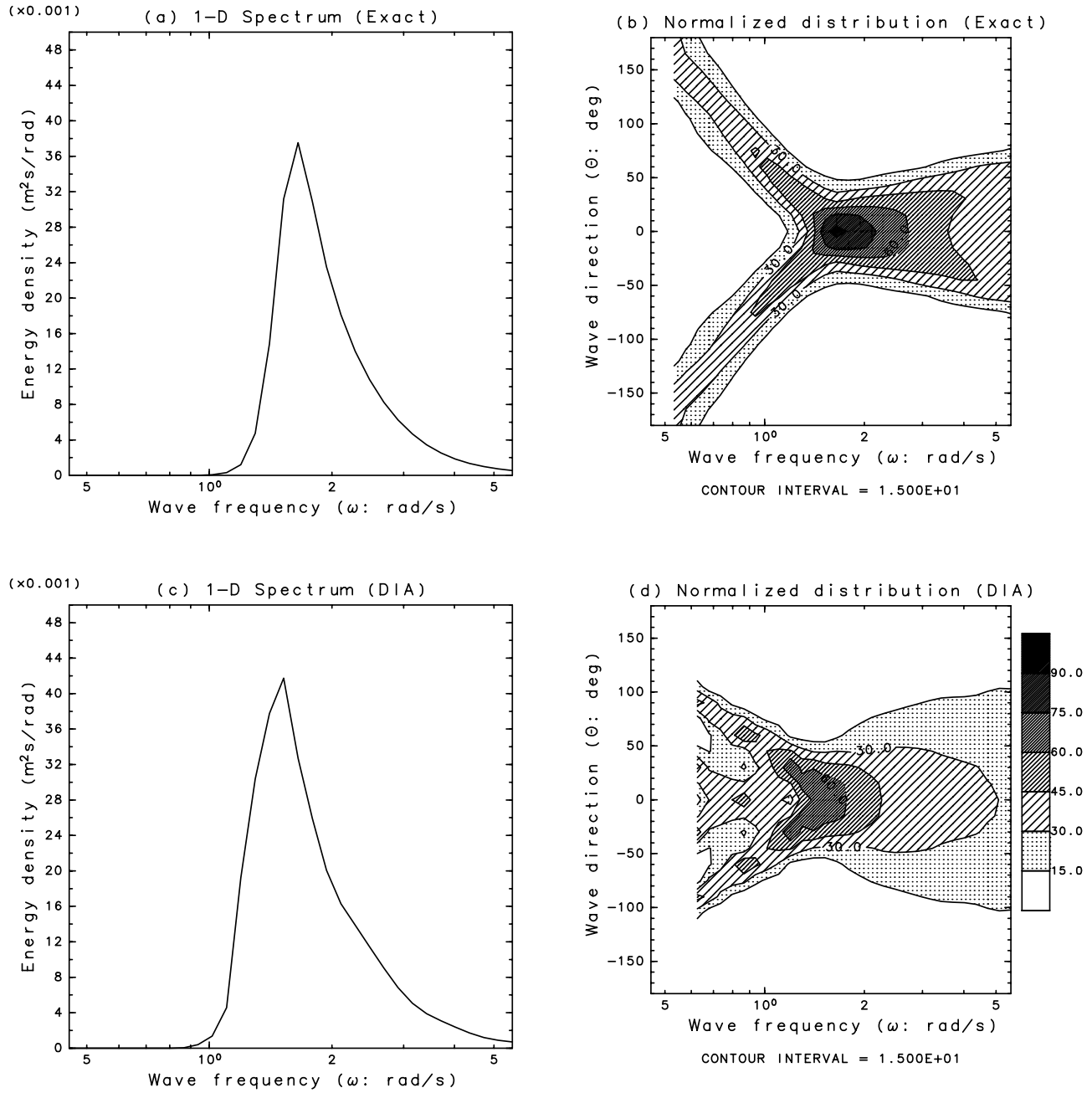

Figure 4. Examples of wave spectra. (a) Frequency spectrum $E(\omega)$ and (b) normalized directional distribution $D(\omega, \theta)$ ($\times 100$) from the exact computation. (c) same as Figure 4a but from the DIA, and (d) same as Figure 4b but from the DIA.

wave directions (θ_S) is large on 17 April, 19 April, and 27 April.

6. Wave Parameter Comparisons

6.1. Comparison of Wave Heights

[41] Figure 6 shows examples of the comparison of significant wave heights. The comparisons for various a_w in equation (32) are summarized in Figure 7. The correlation coefficients ($r_c(H_n, H_p)$) between wave heights at Ng (H_n) and predicted wave heights (H_p) are larger than correlation coefficients ($r_c(H_k, H_p)$) between wave heights at Ky (H_k) and predicted wave heights (H_p). The RMS difference ($\Delta_r(H_n, H_p)$) between H_n and H_p is also smaller than the RMS difference ($\Delta_r(H_k, H_p)$) between H_k and H_p, because station Ky in Figure 2 is more affected by the local topography. The RMS difference $\Delta_r(H_n, H_p)$ is the smallest at $a_w = 1.5$ for the exact calculation, while $\Delta_r(H_n, H_p)$ is the smallest at $a_w = 1.3$ for the DIA. The value of $r_c(H_k, H_p)$ for the DIA is larger than that for the exact computation, and $\Delta_r(H_n, H_p)$ for the DIA is smaller. The wave heights tend to be underestimated from 9 May 1998, especially for the exact computation (Figure 6).

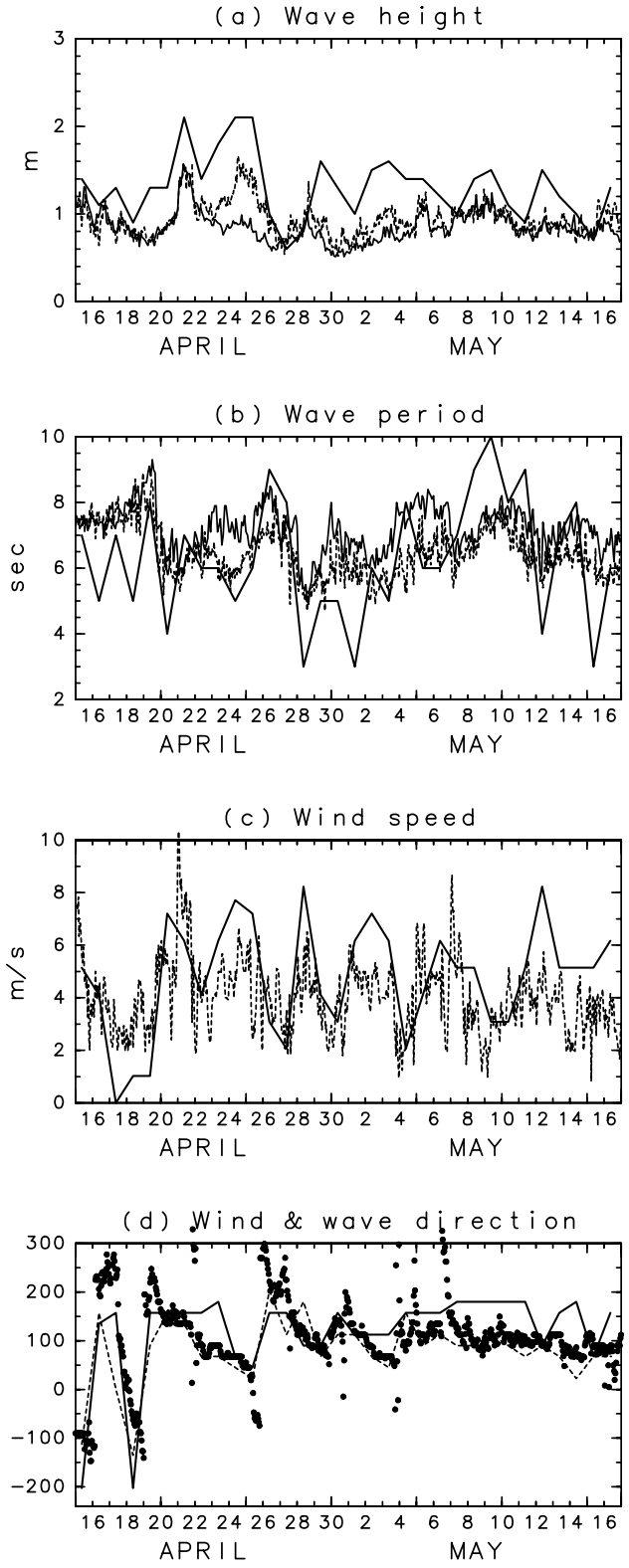

Figure 5. Time series of (a) wave heights at Kyan (thin solid line: Ky in Figure 2) and Nakagusuku (thin dotted line: Ng in Figure 2) and 26°N, 128°E (thick solid line: P in Figure 2); (b) same as Figure 5a but for wave periods; (c) hourly wind speeds at Itokazu (thin dotted line: I in Figure 2), and 26°N, 128°E (thick solid line: P in Figure 2); and (d) wind directions at I (θ_I: black circle) and P (θ_W: thin dotted line), and wave directions at P (θ_S: thick solid line).

6.2. Comparison of Directional Distributions

[42] Figure 8 shows directional distributions $D(\theta) = D(\omega_B, \theta)$ at 2 JST on 27 April and 0 JST on 27 April, when wind speeds are large (Figure 5c), and wind-wave signal might dominate over any background swell. The model-predicted directional distribution $D(\theta)$ from the DIA is closer to the radar-estimated directional distribution than that from the exact computation in Figure 8a. The directional distribution $D(\theta)$ from the exact computation is narrower than radar-estimated directional distribution. The difference between radar-estimated directional distribution from the two-parameter model and that from the four-parameter model is not so large in Figure 8a.

[43] The model-predicted directional distribution $D(\theta)$ from the DIA is close to the radar-estimated directional distribution using the two-parameter model in Figure 8b. The difference of radar-estimated directional distributions in Figure 8b is larger than that in Figure 8a. The pair of the best agreement between radar-estimated directional distributions and model-predicted directional distributions changes with time.

[44] Figure 9 shows examples of the time series of the normalized directional distribution $D(\theta) = D(\omega_B, \theta)$. The area-averaged radar-estimated directional distributions are shown in Figures 9a and 9b, and are expressed by equation (5). The wave model-predicted directional distributions are estimated on the basis of predicted wave spectrum $F(\omega, \theta)$ by dividing frequency spectrum $E(\omega)$., i.e., $D(\theta) = F(\omega_B, \theta)[E(\omega_B)]^{-1}$.

[45] The examples of the model-predicted directional distributions shown in Figures 9c and 9d are those for $a_w = 1.4$ in equation (32). The value of $a_w = 1.4$ lies between $a_w = 1.3$ and $a_w = 1.5$: The $a_w = 1.3$ is the optimal value of a_w to predict wave height using the DIA (section 6.1, Figure 7) and $a_w = 1.5$ is the optimal value of a_w to predict wave height using the exact computation (section 6.1, Figure 7).

[46] The radar-estimated area-averaged directional distributions $D(\theta)$ for the two-parameter model ($L = 1$ in equation (5)) are broader than those for the four-parameter model (Figures 9a and 9b). Even in the four-parameter model, most of the directional distributions are unimodal (Figure 9b). The directional distributions are not symmetric with respect to the mean direction in the four-parameter model. It has been shown that the AIC (Akaike's Information Criterion) is useful in selecting the model function [*Hisaki*, 2004]. The four-parameter model is more accurate to describe directional distributions based on the AIC. The directional distributions $D(\theta)$ are accurately predicted by the wave model, and those from the exact computation (Figure 9c) are narrower than those from the DIA (Figure 9d). Because the directional distributions are not symmetric with respect to the mean direction, the directional distribution in the two-parameter model ($L = 1$ in equation (5)) are broader than that in the four-parameter model. However, it is difficult to discern a more useful parameterization for predicting directional distributions from exact computation or from the DIA shown in Figure 9. The quantitative evaluation of the directional distribution comparison will be described by comparing the first- and the second-order moments of directional distributions.

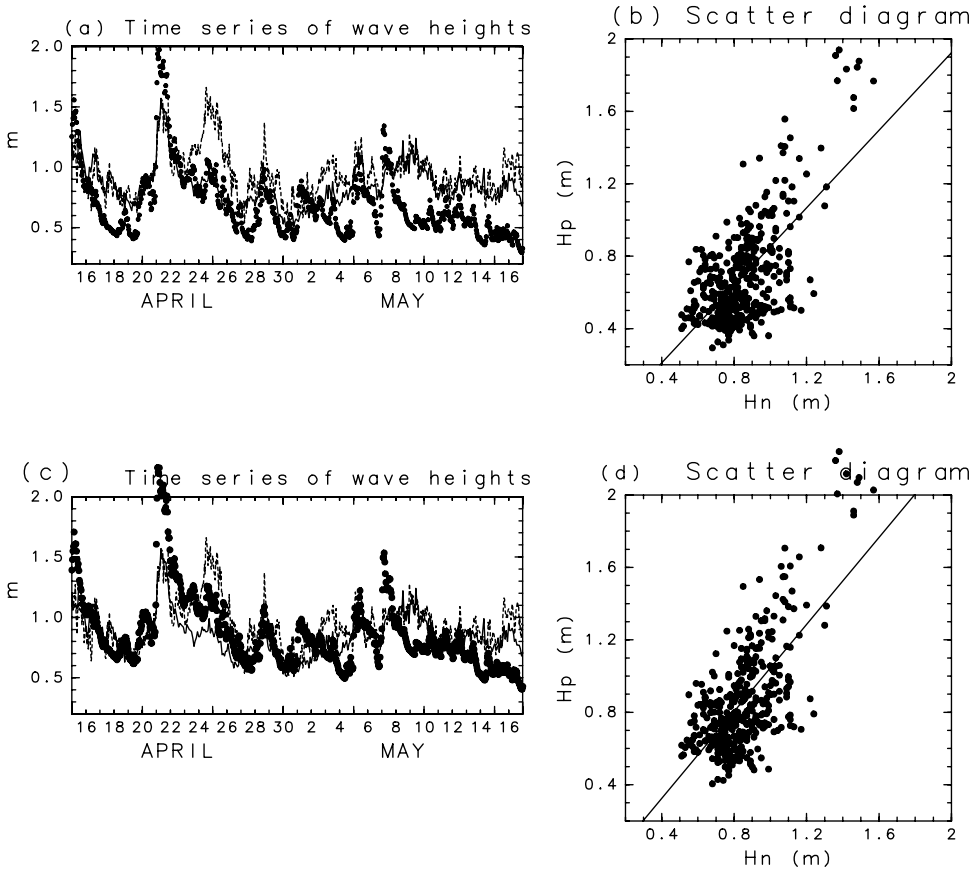

Figure 6. (a) Time series of observed significant wave heights at Kyan (thin solid line) and at Nakagusuku (thin dotted line) and predicted significant wave heights from the exact computation for $a_w = 1.4$. (b) Scatter diagram between wave heights at Nakagusuku and significant wave heights from the exact computation. (c) Same as Figure 6a but for the DIA. (d) Same as Figure 6b but for the DIA.

6.3. First-Order Moment

[47] Figure 10 shows a comparison between area-averaged radar-estimated wave direction with respect to the wind direction ($\theta_{mr} - \theta_I$) and wave model-predicted mean wave direction with respect to the wind direction at station I ($\theta_{mp} - \theta_I$). Note that the correlation of the of direction values is dependent on how they are measured, because direction values are determined by the measurement method: The direction value is determined from the 0° direction and in terms of how the positive value of the direction is defined. In the example of Figures 10a and 10d, the eastward direction is 0° and the northward direction is 90°.

[48] If the short-wave directions with the Bragg wavelength are changed simultaneously with the change of wind direction, the correlation between area-averaged radar-estimated mean wave directions with respect to wind directions and wave model-predicted mean wave directions with respect to wind directions ($r_c(\theta_{mp} - \theta_I, \theta_{mr} - \theta_I)$) would be low. If the wave direction change associated with a sudden wind shift can be reproduced, the correlation $r_c(\theta_{mp} - \theta_I, \theta_{mr} - \theta_I)$ would be high. The comparisons are summarized in Figure 11. The RMS differences ($\Delta_r(\theta_{mp}, \theta_{mr})$) between the model-predicted and the radar-estimated wave directions for the four-parameter model ($L = 2$ in equation (5)) are smaller than those for the two-parameter model ($L = 1$ in equation (5)). The correlations between the radar-estimated short-wave directions and the predicted short-wave directions using the exact computation are higher than those from the DIA. The RMS difference between radar-estimated short-wave directions and model-predicted short-wave directions using the exact computation is smaller than the RMS difference between wind directions at station I and radar-estimated short-wave directions at the closest grid point to the station I [*Hisaki*, 2002], although the radar-estimated short-wave directions shown in Figure 10 are area-averaged short-wave directions.

[49] Many of the outliers in the scatter diagram plotting wind directions at station I and radar-estimated short-wave directions are related to shifts in wind direction [*Hisaki*, 2002, Figure 5]. Some outliers have been removed from *Hisaki*'s [2002] Figure 5. The number of outliers in the scatter plot are decreased in Figure 10 compared with *Hisaki*'s [2002] Figure 5.

6.4. Second-Order Moment

[50] Figure 12 shows a the comparison between the area-averaged radar-estimated second-order moment of short-wave directional distribution ($\sigma_{\theta r} = \sigma_\theta(\omega_B)$) and the predicted directional distribution ($\sigma_{\theta p} = \sigma_\theta(\omega_B)$), where the second-order moment of the short-wave directional distribution is calculated from equation (10). The predicted second-order moment of short-wave directional distribution

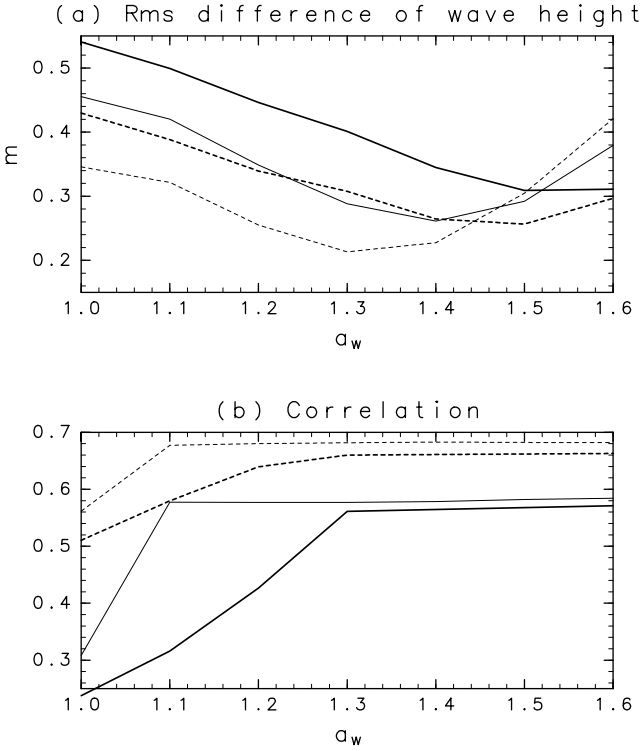

Figure 7. Comparisons of predicted wave heights from the exact computation and the DIA with observed wave heights at Kyan and Nakagusuku for various a_w in equation (32). (a) RMS difference $\Delta_r(H_k, H_p)$ for the exact computation (thick solid line), $\Delta_r(H_n, H_p)$ (thick dotted line) for the exact computation, $\Delta_r(H_k, H_p)$ for the DIA (thin solid line), and $\Delta_r(H_n, H_p)$ (thin dotted line) for the DIA. (b) Same as Figure 7a but for correlation coefficients.

($\sigma_{\theta p}$) using the exact computation is smallest in Figures 12a and 12d, which shows that the predicted directional distribution from the exact computation is the narrowest.

[51] The radar-estimated second-order moments of short-wave directional distributions ($\sigma_{\theta r}$) based on the four-parameter model (L = 2 in equation (5)) are seen to be correlated with model predicted second-order moments ($\sigma_{\theta p}$) in both Figure 12c (exact computation) and Figure 12f (DIA). On the other hand, the radar-estimated second-order moments of short-wave directional distributions using the two-parameter model (L = 1 in equation (5)) are seen to be correlated with model predicted second-order moments ($\sigma_{\theta p}$) in neither Figure 12b (exact computation) nor Figure 12e (DIA).

[52] In order to investigate the effect of the swell on the short-wave direction, the observation period is divided into two categories: One is referred to as "swell time" and another period is referred to as "wind-wave time." The wind-wave time is the time within 12 hours of $|\theta_S - \theta_W| \leq 45°$ in Figure 5d, where θ_S and θ_W are JMA-analyzed wave directions and wind directions, respectively. Otherwise the time is referred to as swell time.

[53] Figure 13 shows the summary of a comparison between the radar-estimated second-order moments of short-wave directional distributions ($\sigma_{\theta r}$) from the four-parameter model (L = 2 in equation (5)) for various a_w in equation (32).

[54] Although the correlations between radar-estimated second-order moments and model-predicted second-order moments ($r_c(\sigma_{\theta r}, \sigma_{\theta p})$) using the exact computation are higher than those from the DIA, the RMS differences $\Delta_r(\sigma_{\theta r}, \sigma_{\theta p})$ between them are larger for the exact computation. The predicted second-order moments from the exact computation are smaller than the radar-estimated second-order moments. The correlation $r_c(\sigma_{\theta r}, \sigma_{\theta p})$ for the swell time is significantly larger than that for the wind-wave time, because the second-order moments in the swell time is larger than those in the wind-wave time.

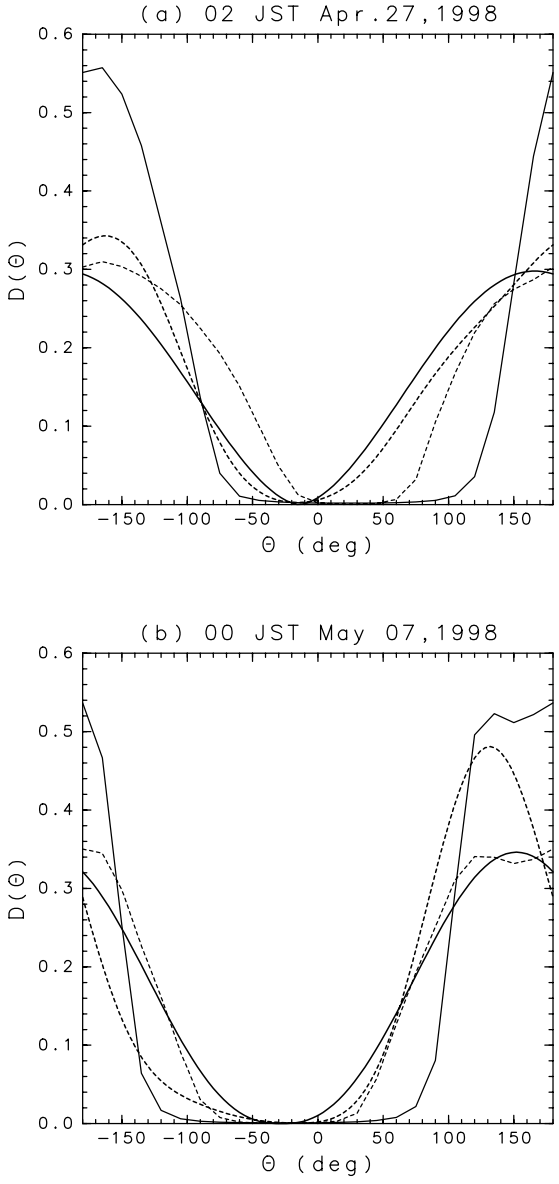

Figure 8. Radar-estimated normalized directional distributions $D(\theta) = D(\omega_B, \theta)$ from the two-parameter model (thick solid line) and from the four-parameter model (thick dotted line), and model-predicted $D(\theta)$ from the exact computation (thin solid line) and from the DIA (thin dotted line) for a_w = 1.4 at (a) 2 JST on 27 April 1998 and (b) 0 JST on 7 May 1998.

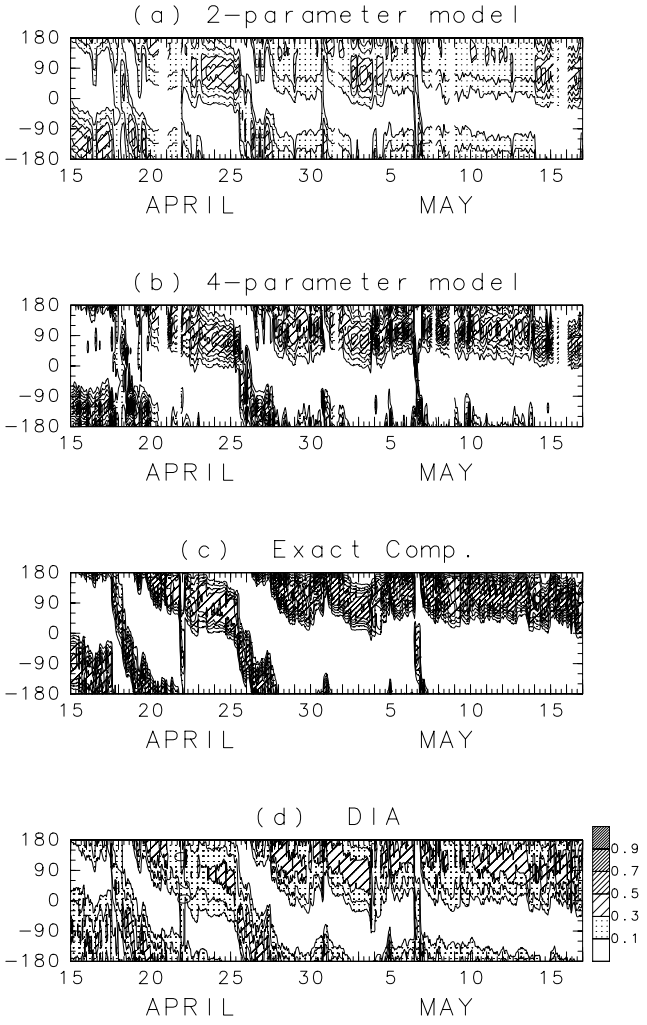

Figure 9. Normalized directional distribution $D(\theta) = D(\omega_B, \theta)$ (a) from radar estimation and the two-parameter model ($L = 1$ in equation (5)), (b) from radar estimation and the four-parameter model ($L = 2$ in equation (5)), (c) predicted from the exact computation for $a_w = 1.4$, and (d) same as Figure 9c but from the DIA.

[55] *Wyatt et al.* [1997] compared radar-estimated directional short-wave distributions (second-order moments) with in situ observations. Although the correlation coefficient between them was not shown, the plots of radar-estimated directional short-wave distributions and in situ observations in the scatter diagram were scattered as shown in Figure 12.

[56] Figure 14 shows relationships between normalized Bragg frequencies by peak frequencies (ω_B/ω_m) and second-order moments of short-wave distributions. The second-order moments of unimodal distributions by Mitsuyasu-Hasselmann type ($\cos^{2s}((\theta - \beta_1)/2)$ form, where s is given by equation (31) [*Mitsuyasu et al.*, 1975; *Hasselmann et al.*, 1980]) and by Donelan-type ($\mathrm{sech}^2(\beta(\theta - \beta_1))$ form, where β is given by *Donelan et al.* [1985]) are also shown in Figure 14. The Donelan-type empirical equation is extended to $\omega/\omega_m \geq 1.6$ ($\log(\omega/\omega_m) \geq 0.47$).

[57] Figures 14a and 14b shows relationships between normalized Bragg frequency by peak frequencies and the second-order moments of short-wave distributions ($\sigma_{\theta p}$) predicted from the exact computation and the DIA, respectively. The peak radian wave frequencies ω_m in Figures 14a and 14b are also predicted from the exact computation and the DIA, respectively. The second-order moments become larger as higher ω_B/ω_m, which are consistent with Mitsuyasu-Hasselmann-type and Donelan-type directional distributions. However, the plots of $\log(\omega_B/\omega_m)$ and $\sigma_{\theta p}$ in Figures 14a and 14b are scattered compared with Figure 4, because winds are not stationary. In particular, plots in the swell time (white circles (◯) in Figure 14) are scattered. The values of the second-order moments ($\sigma_{\theta p}$) predicted from the DIA are closer to those from Mitsuyasu-Hasselmann-type and Donelan-type directional distributions than those predicted from the exact computation.

[58] Figures 14c and 14d show relationships between normalized Bragg frequency by predicted peak frequencies (ω_B/ω_m) and the radar-estimated second-order moments of short-wave distributions ($\sigma_{\theta r}$) from the two- and four-parameter models, respectively. The peak wave frequencies ω_m are predicted from the exact computation: The difference between ω_m from the exact computation and ω_m from the DIA is small. The tendency that the second-order moments become larger as higher wave frequencies can be seen in both Figures 14c and 14d. The second-order moments derived from Mitsuyasu-Hasselmann-type and Donelan-type directional distributions are closer to values of the $\sigma_{\theta r}$ estimated from the four-parameter model (Figure 14d) than those from the two-parameter model (Figure 14c). The plots in Figures 14c and 14d are scattered. Some second-order moments in the swell time are large in Figures 14c and 14d (white circles (◯)). Most of the cases that radar-estimated second-order moments $\sigma_{\theta r}$ are much larger than second-order moments derived from Mitsuyasu-Hasselmann-type and Donelan-type directional distributions are in the swell time because of wind shifts.

7. Horizontal Variability

7.1. Gridded Wave Parameters

[59] In section 6, the radar-estimated short-wave directional distributions were obtained from area-averaged short-wave directional parameters. The area-averaged short-wave parameters were estimated from many Doppler spectra on radial grids as seen in Figure 2 (black circles in Figure 2). These wave parameters were estimated by seeking the minima of L_g (equation (6)) as explained in section 2. The relationship between the model-prediction error and the homogeneity of wave field is explored.

[60] The wave parameters s and β_1 without area averaging for the two-parameter model ($L = 1$ in equation (5)) could be estimated on the regular grid points by solving equation (4) as explained in section 2. The mean short-wave direction at the grid point is $\theta_m = \beta_1$, and the second-order moment at the grid point is calculated from s using equation (10).

[61] The short-wave parameters in the two-parameter model estimated on each grid point are referred as the gridded mean wave direction (gridded $\theta_{mr} = \theta_m(\omega_B)$) and gridded second-order moment (gridded $\sigma_{\theta r} = \sigma_\theta(\omega_B)$). The meanings of the area-averaged gridded $\sigma_{\theta r}$ and area-

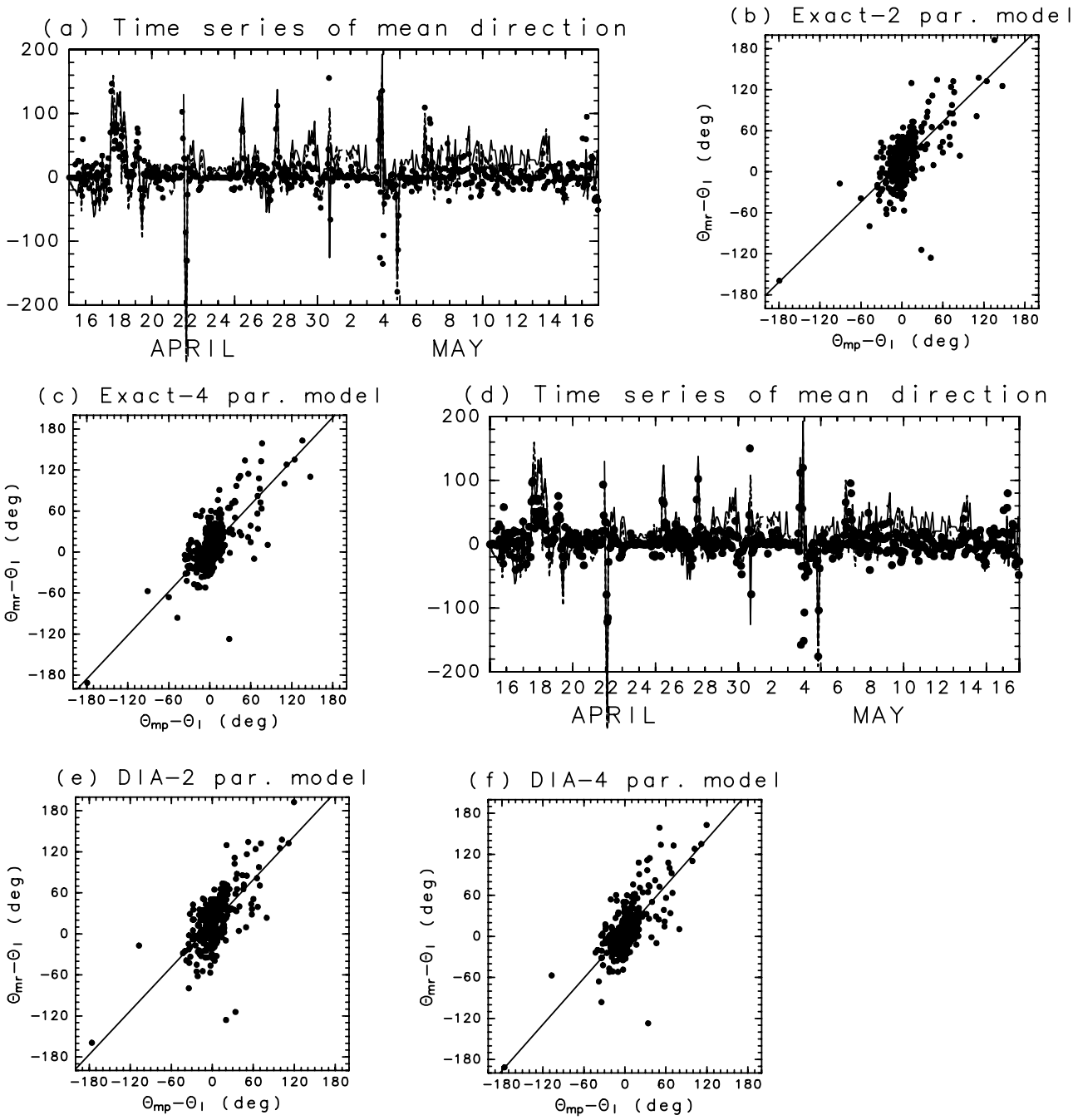

Figure 10. (a) Time series of model-predicted short-wave directions with respect to θ_I (degrees) for the exact computation and $a_w = 1.3$ (black circle), radar-estimated short-wave directions with respect to θ_I from the two-parameter model (thin solid line), and radar-estimated short-wave direction with respect to θ_I from the four-parameter model (thick dotted line), where θ_I is the wind direction at the station I in Figure 2. (b) Scatter diagram between model-predicted short-wave directions with respect to θ_I ($\theta_{mp} - \theta_I$) for the exact computation and $a_w = 1.3$ and radar-estimated short-wave directions with respect to θ_I ($\theta_{mr} - \theta_I$) from the two-parameter model, (c) same as Figure 10b but radar-estimated short-wave directions are for the four-parameter model, (d) same as Figure 10a but model-predicted short-wave directions are for the DIA, (e) same as Figure 10b but model-predicted short-wave directions are for the DIA, and (f) same as Figure 10c but model-predicted short-wave directions are for the DIA.

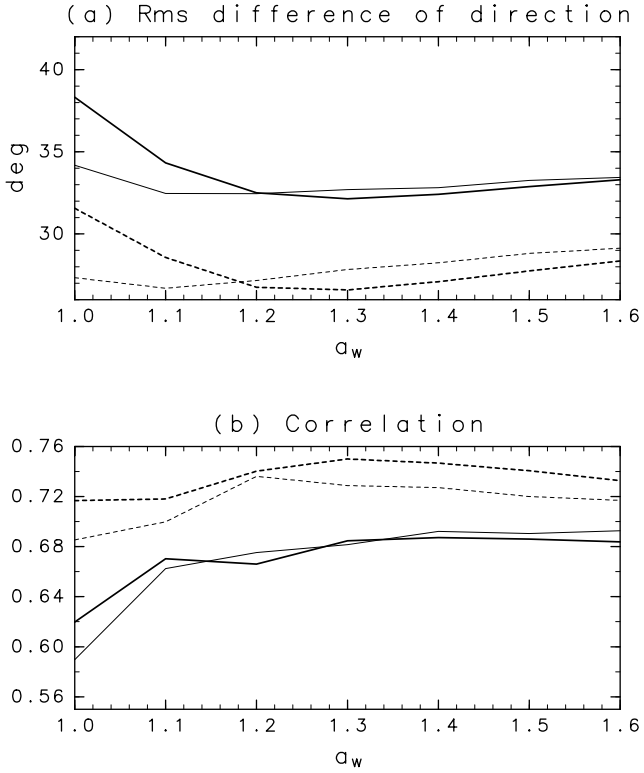

Figure 11. Comparisons of predicted short-wave directions with radar-estimated short-wave directions for various a_w. (a) RMS difference ($\Delta_r(\theta_{mp}, \theta_{mr})$) between model-predicted first-order moments (θ_{mp}) and radar-estimated first-order moments (θ_{mr}) for the exact computation and the two-parameter model (thick solid line), for the exact computation and the four-parameter model (thick dotted line), for the DIA and the two-parameter model (thin solid line), and for the DIA and the four-parameter model (thin dotted line). (b) Same as Figure 11a but for correlation coefficients.

averaged $\sigma_{\theta r}$ are different from each other. The former is explained in section 7.2, and the latter is discussed in section 6.4. The area-standard deviation of gridded $\sigma_{\theta r}$, the area-averaged gridded $\sigma_{\theta r}$, and the area-averaged $\sigma_{\theta r}$ also have different meanings.

7.2. Index of Horizontal Variability

[62] Figure 15a shows a time series of area-averaged gridded $\sigma_{\theta r} = \sigma_\theta(\omega_B)$ (radar-estimated second-order moment of short-wave directional distributions) on regular grid points (crosses in Figure 2). The gridded $\sigma_{\theta r}$ on the grid points are averaged in the HF radar observation area at each 2-hour interval. Figure 15b shows the area-standard deviations of gridded $\sigma_{\theta r}$ estimated using HF radars: The standard deviations in the HF radar observation area are calculated using gridded $\sigma_{\theta r}$ on grid points at 2-hour intervals. Similarly, the area-standard deviations of gridded θ_{mr} (radar-estimated first-order moment of short-wave directional distributions) can be calculated at 2-hour intervals. Figure 15c shows a scatter diagram between the area-standard deviations of gridded θ_{mr} and the area-standard deviations of gridded $\sigma_{\theta r}$.

[63] The time series of the area-averaged values of gridded θ_{mr} estimated using the HF radar is indicated in Figure 7 in a previous paper [*Hisaki*, 2002], and it is not shown here. The area-standard deviations of gridded θ_{mr} were large when the winds or short-waves significantly changed their directions [*Hisaki*, 2002]. The time series of the area-averaged values of gridded $\sigma_{\theta r}$ (Figure 15a) are similar to radar-estimated area-averaged $\sigma_{\theta r}$ from the two-parameter model (Figures 12a and 12d, thin solid line). The area-averaged values of gridded $\sigma_{\theta r}$ are estimated by area-averaging the gridded $\sigma_{\theta r}$ estimated on each regular grid point. The radar-estimated values of area-averaged $\sigma_{\theta r}$ are estimated directly using all of the first-order ratios (r_i in equation (4)) employing the method explained in section 2.

[64] The temporal variation of standard deviations of gridded $\sigma_{\theta r}$ at each 2-hour interval ranges from 5° to 15° in Figure 15b. There are no correlations between the area-averaged values of gridded $\sigma_{\theta r}$ (Figure 15a) and the area-standard deviations of gridded $\sigma_{\theta r}$ (Figure 15b). The area-standard deviations of gridded θ_{mr} are large when the standard deviations of gridded $\sigma_{\theta r}$ are large (Figure 15c). They are correlated with a correlation coefficient of 0.61. Because of this correlation, it is possible to use only the area-standard deviation of $\sigma_{\theta r}$ as an index of the horizontal variability of the short-wave directional distributions in the HF radar observation area.

7.3. Relationship Between Horizontal Variability and Model-Prediction Error

[65] Figure 16 is the scatter diagram between area-standard deviation of gridded $\sigma_{\theta r}$ and area-averaged $|\sigma_{\theta r} - \sigma_{\theta p}|$ for $a_w = 1.4$ in equation (32). The area-standard deviation of gridded $\sigma_{\theta r}$ is the index of the horizontal variability. The value of $|\sigma_{\theta r} - \sigma_{\theta p}|$ is the difference between the radar-estimated second-order moment and the model-predicted second-order moment. The value of $\sigma_{\theta r}$ in area-averaged $|\sigma_{\theta r} - \sigma_{\theta p}|$ is obtained from the four-parameter model. This figure shows the relationship between horizontal variability of short-wave fields and the model-prediction error of second-order moments. In many cases, the large values of area-averaged $|\sigma_{\theta r} - \sigma_{\theta p}|$ are associated with horizontal variabilities of short-wave fields: Both the area-standard deviation of gridded $\sigma_{\theta r}$ (horizontal axis in Figure 16) and area-averaged $|\sigma_{\theta r} - \sigma_{\theta p}|$ (vertical axis in Figure 16) are large. In this example ($a_w = 1.4$), these cases are evident in the exact computation (Figure 16a). However, cases in which the large values of area-averaged $|\sigma_{\theta r} - \sigma_{\theta p}|$ are associated with large area-standard deviations of gridded $\sigma_{\theta r}$ are not evident in the exact computation for other values of a_w.

[66] The correlations between the model-prediction errors of wave heights ($|H_p - H_k|$) and model-prediction errors of short-wave directional distributions ($|\sigma_{\theta r} - \sigma_{\theta p}|$) are investigated, where H_p is the model-predicted wave height and H_k is the wave height observed at station Ky in Figure 2. There are almost no correlations between them. For example, the correlation coefficient between $|H_p - H_k|$ and $|\sigma_{\theta r} - \sigma_{\theta p}|$ is $r_c(|H_p - H_k|, |\sigma_{\theta r} - \sigma_{\theta p}|) = 0.07$, where $\sigma_{\theta p}$ and H_p are respectively the model-predicted second-order moment and wave height from the exact computation for $a_w = 1.4$ in equation (32), and $\sigma_{\theta r}$ is the radar-estimated second-order moment from the four-parameter model. The

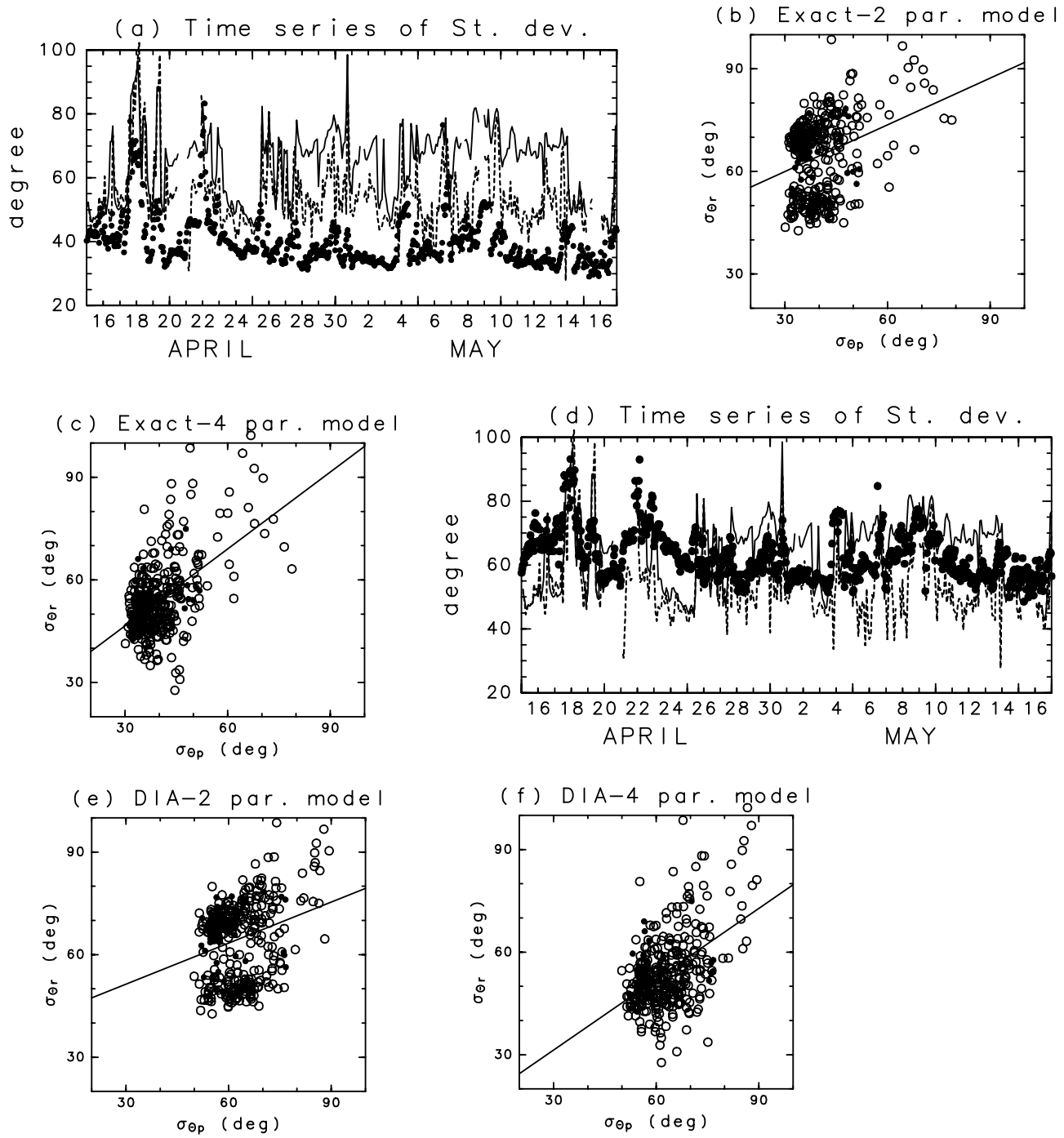

Figure 12. (a) Time series of predicted second-order moments of short-wave directional distributions ($\sigma_{\theta p} = \sigma_\theta(\omega_B)$) for the exact computation and $a_w = 1.3$ (black circle), radar-estimated area averaged radar-estimated second-order moments ($\sigma_{\theta r} = \sigma_\theta(\omega_B)$) from the two-parameter model (thin solid line), and radar-estimated second-order moments from the four-parameter model (thick dotted line). (b) Scatter diagram between $\sigma_{\theta p}$ (horizontal axis) for the exact computation and $a_w = 1.3$ and $\sigma_{\theta r}$ (vertical axis) from the two-parameter model. White circles indicate swell time and black circles indicate wind-wave time. (c) Same as Figure 12b but for the four-parameter model, (d) same as Figure 12a but for the DIA, (e) same as Figure 12b but for the DIA, and (f) same as Figure 12c but for the DIA.

correlation coefficient $r_c(|H_p - H_k|, |\sigma_{\theta r} - \sigma_{\theta p}|)$ is 0.17, where $\sigma_{\theta p}$ and H_p are from the DIA and $\sigma_{\theta r}$ is from the four-parameter model. The main error source of the model wave height prediction differs from that of the model's short-wave distribution prediction. The wave height prediction error is due mainly to the omission of the propagation term, because the swell propagation is not considered. The short-wave directional distribution prediction error is due mainly to the

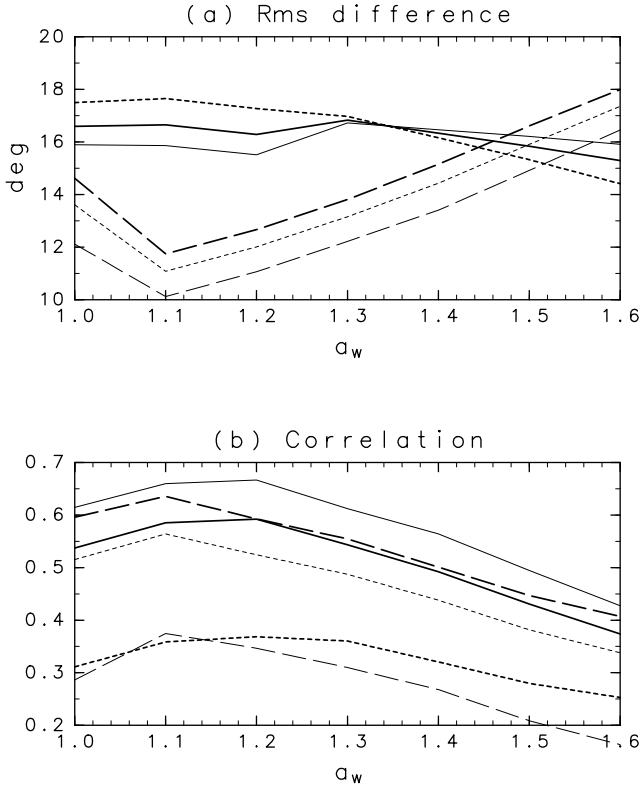

Figure 13. Comparisons of predicted short-wave second-order moments for the four-parameter model with radar-estimated short-wave second-order moments for various a_w. (a) RMS difference $\Delta_r(\sigma_{\theta p}, \sigma_{\theta r})$ for the exact computation (thick solid line), for the exact computation and the wind-wave time (thick dotted line), for the exact computation and the swell time (thin solid line), for the DIA (thin dotted line), for the DIA and the wind-wave time (thin dashed line), and for the DIA and the swell time (thick dashed line). (b) Same as Figure 13a but for correlation coefficients.

error of winds and the parameterization of source functions as such S_{in} (equation (11)) and S_{ds} (equation (16)).

8. Discussion and Conclusion

[67] The short-wave directional distributions estimated by the HF radar are compared with the model predictions using both the exact computation of $S_{nl}(\omega, \theta)$ and the DIA. The comparisons in this study are as follows: (1) comparison of predicted wave spectra from the DIA and those from the exact computation, (2) comparison of radar-estimated short-wave directional distributions of the two-parameter model with those of the four-parameter model, (3) comparison between radar-estimated first-order moments of short-wave directional distributions and those predicted by wave model for both the DIA and the exact computation, and (4) comparison between radar-estimated second-order moments of short-wave directional distributions and those predicted from wave model for both the DIA and the exact computation.

[68] Because it is not feasible to compute equation (1) for the exact computation, wave spectra are predicted using equation (2) for both the exact computation and the DIA. In addition, the wind data on the sea surface is not available, and wind inputs are expressed as equation (32) for various a_w.

[69] The assumptions of these calculations are as follows: Wave fields are almost statistically homogeneous in the HF radar observation area. Wind waves rather than the swells propagating from the distance are dominant.

[70] The former assumption is related to the omission of the propagation term in equation (1). The latter assumption is related to the prediction of the source function S_t in equation (1). The validities of the assumptions are investigated.

[71] For the exact computation, methods to compute the nonlinear interaction source function $S_{nl}(\omega, \theta)$ and derivatives with respect to the wave spectrum $\partial S_{nl}(\omega, \theta)/\partial F(\omega_p, \theta_p)$ are developed. The numerical integration using this method is stable. The effect of the singularities at $S_0 = 0$ in equation (A6) and the effect of the low direction resolution ($M = 24$) on the numerical integration can be reduced.

[72] The accuracy of wave heights predicted using the DIA is greater than that derived from the exact computation, because the parameters in the DIA such as λ_{nl} in equation (26) and C_0 in equation (28) along with the parameterizations of S_{in} and S_{ds} are tuned to predict wave heights. The predicted wave directional distributions determined using the exact computation are narrower than those obtained by the DIA at higher frequencies.

[73] The intercomparison between radar-estimated directional distributions and the model predictions shows that the four-parameter model for radar estimation is more effective than the two-parameter model.

[74] It has also found that the four-parameter model is more effective than the two-parameter model not only on the basis of the AIC [*Hisaki*, 2002], but also on the basis of a comparison of these models in terms of their predictions. The short-wave directional distributions are not symmetric with respect to the mean direction; therefore, the directional distributions described by the two-parameter model ($L = 2$ in equation (5)) are broader than those obtained by the four-parameter model.

[75] The first- and the second-order moments of radar-estimated short-wave directional distributions are compared with those predicted using the exact computation and the DIA. The model predicted first-order moments with respect to the wind directions are closely correlated with first-order moments estimated using HF radar with respect to wind directions. This result shows that the change in short-wave direction associated with a sudden shift of wind can be reproduced in both the exact computation and the DIA. *Georges et al.* [1993] estimated wind directions associated with a moving hurricane using HF radar, although the time lag of the short-wave response to a wind shift was not considered. The incorporation of the wave prediction model for estimating wind direction through the use of HF radar is the next subject of this study, because the time lag of the short-wave response to a wind shift can be considered.

[76] The model-predicted second-order moments of short-wave directional distributions are also correlated with those estimated using HF radar. The wind directions are time variable, and the short-wave directional distributions are asymmetrical with respect to wind direction. The correlation

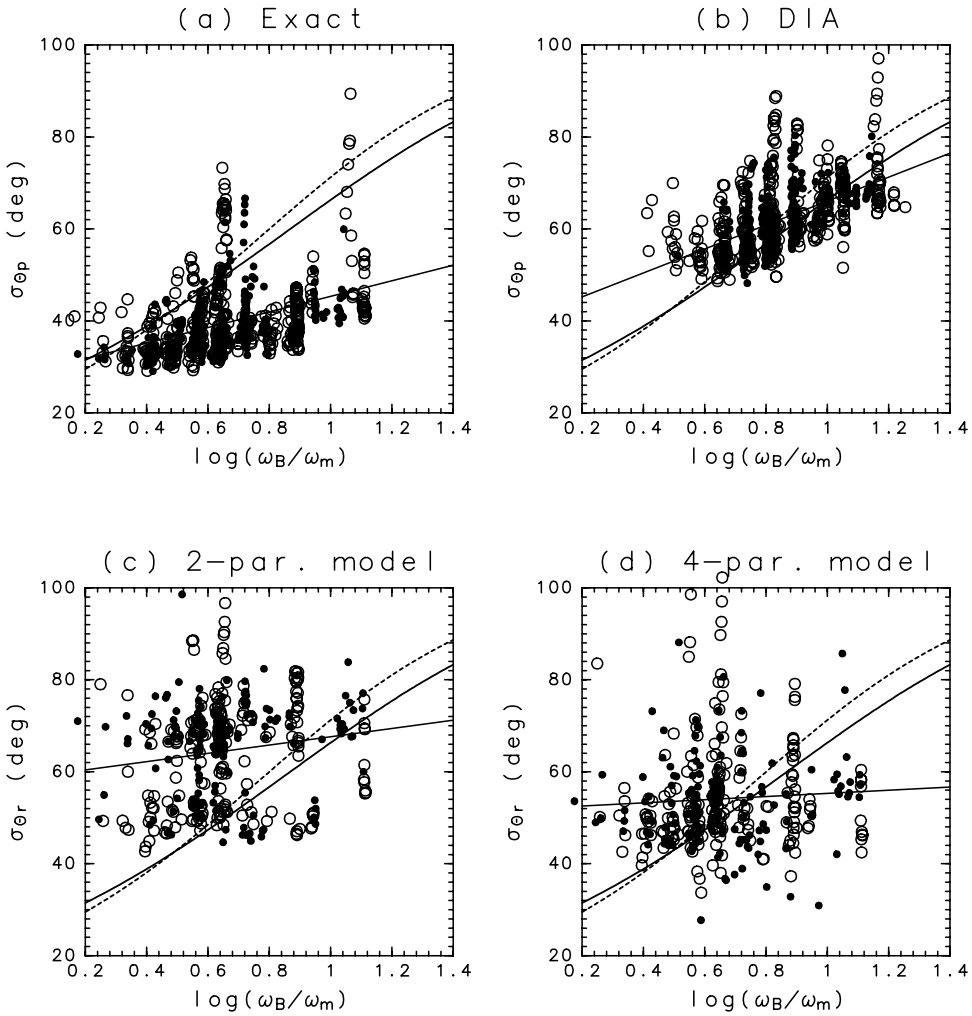

Figure 14. Scatter diagram between $\log(\omega_B/\omega_m)$ and second-order moments σ_θ. (a) Predicted from the exact computation, and (b) predicted from the DIA. (c) Peak radian frequencies ω_m predicted from the exact computation and σ_θ, the radar-estimated second-order moments from the two-parameter model. (d) Same as Figure 14c but from the four-parameter model. White circles indicate swell time and black circles indicate wind-wave time. Thick solid line, σ_θ as a function of $\log(\omega/\omega_m)$ by Mitsuyasu-Hasselmann type distribution (equation (31)); thick dotted line, σ_θ as a function of $\log(\omega/\omega_m)$ by Donelan-type distribution; thin solid line, regression line.

for the swell time is larger than that for the wind-wave time. If the change of wind direction is not significantly large, the short-wave direction changes smoothly. If the change of wind direction is large, the peak of the short-wave directional distribution in the new wind direction grows, while the old peak of the short-wave directional distribution decays [*Young et al.*, 1987]. The result in which model-predicted second-order moments of short-wave directional distributions are correlated with those estimated using HF radar implies that these transient short-wave directional distributions associated with changes in wind direction can be reproduced by the model.

[77] The short-wave directional distributions predicted by the exact computation are narrower than those by both the DIA and the radar. The correlation of radar-estimated second-order moments with those predicted by the exact computation is higher than that with those predicted by the DIA. However, the RMS difference between the radar-estimated second-order moments and those predicted by the model ($\Delta_r(\sigma_{\theta r}, \sigma_{\theta p})$) using the exact computation is larger than that from the DIA.

[78] The relationship between horizontal variabilities and the predictions of short-wave directional distributions were investigated. There is not a clear relationship between them. Although there may be some cases in which prediction errors are associated with horizontal variabilities, horizontal variability is not a primary source of error. The omission of the propagation term is not a main source of prediction error in the short-wave directional distribution.

[79] The effect of the swell on the prediction error is also investigated. The relationship between swells and prediction errors in short-wave directional distributions is also unclear. The main error source of the short-wave distribution pre-

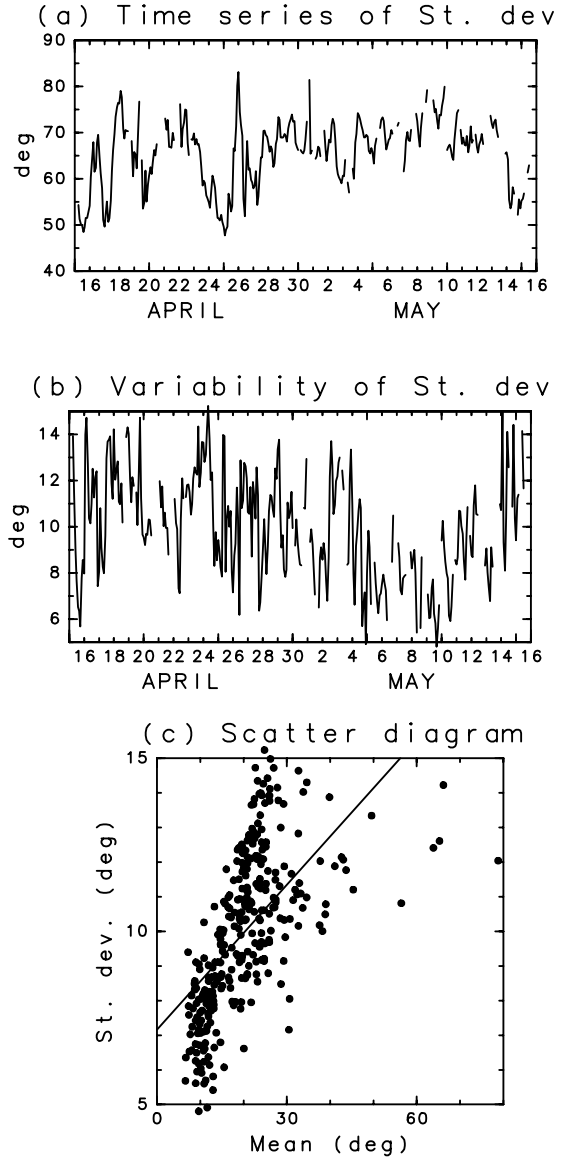

Figure 15. (a) Time series of area-averaged values of gridded $\sigma_{\theta r}$ (radar-estimated second-order moments of short-wave directional distributions) on regular grid points (crosses in Figure 2), (b) area-standard deviations of gridded $\sigma_{\theta r}$ estimated by HF radar, and (c) scatterplot between area-standard deviations of gridded θ_{mr} (radar-estimated first-order moments of short-wave directional distributions: horizontal axis) and area-standard deviations of gridded $\sigma_{\theta r}$ (vertical axis).

diction differs from that of the model's wave height prediction. The swell is not a primary source of error.

[80] The result that predicted wave parameters from the DIA is better than those from the exact computation does not show that the DIA is better than the exact computation. The other source terms (S_{ds} and S_{ds}) in the WAM model are tuned to give good results when the DIA is used. We must improve the other source terms if we use the exact computation or other parameterization of S_{nl} for wave prediction.

[81] In this study, it is assumed that wind over sea surface is a constant multiple of the inland wind speed for an entire period. Therefore the wave prediction should be done using wind data over sea surface in the next study. It is noted that the temporal resolution of wind data is important for predicting second-order moments of short-wave directional distributions, because short-wave directional distributions vary with winds quickly.

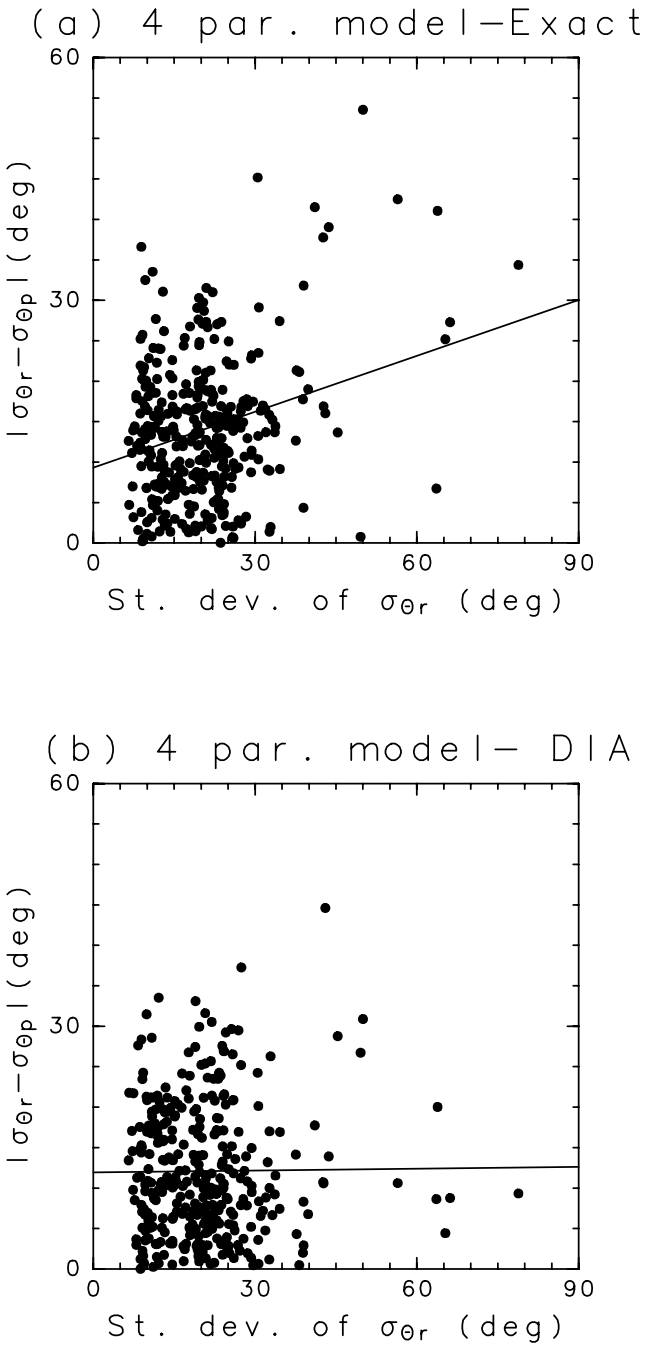

Figure 16. (a) Scatter diagram between area-standard deviation of gridded $\sigma_{\theta r}$ (radar-estimated second-order moments of short-wave directional distributions) from the two-parameter model (horizontal axis) and area-averaged $|\sigma_{\theta r} - \sigma_{\theta p}|$ (vertical axis) from the four-parameter model and exact computation. (b) Same as Figure 16a but from the DIA, where $\sigma_{\theta p}$ is the model-predicted second-order moments.

[82] The correlation of the second-order moments in the swell time is significantly larger that in the wind-wave time, because of the broad wave directional distribution in the swell time. The effects of the swell on the short-wave directional distribution are smaller than prediction errors due to the parameterization of the source function.

[83] The investigation of the effect of the parameterization of S_{in} and S_{ds} on short-wave directional distribution is the next subject of this study. The improvement of the model from equation (2) to equation (1) should be explored.

Appendix A: Numerical Computation of the Four-Wave Interaction

[84] The method used to compute four-wave interaction is based on that reported by *Komatsu and Masuda* [2001]. The source function of the nonlinear interaction is

$$S_{nl}(\omega_4,\theta_4) = \frac{\omega_4 k_4}{C_{g4}} \int\int\int d\mathbf{k}_1 d\mathbf{k}_2 d\mathbf{k}_3 \delta_\omega \delta_k [Hasselmann, 1962], \\ G[N_1 N_2 (N_3 + N_4) - N_3 N_4 (N_1 + N_2)], \tag{A1}$$

where δ_ω and δ_k are delta functions corresponding to the resonance conditions of quadruplets as

$$\omega_1 + \omega_2 = \omega_3 + \omega_4 (\equiv \omega_a) \tag{A2}$$

$$\mathbf{k}_1 + \mathbf{k}_2 = \mathbf{k}_3 + \mathbf{k}_4 (\equiv \mathbf{k}_a), \tag{A3}$$

where $\mathbf{k}_i = (k_i \cos\theta_i, k_i \sin\theta_i)$ (i = 1, ..,4), $\omega_i^2 = g k_i$, $N_i = F(\omega_i, \theta_i) C_{gi}/(\omega_i k_i)$ (i = 1, ..,4) are the wave action densities, $C_{gi} = \partial\omega_i/\partial k_i = g/(2\omega_i)$ (i = 1, 2, 3, 4) are wave group velocities, and $G = G(\omega_1, \omega_2, \omega_3, \omega_4, \theta_1, \theta_2, \theta_3, \theta_4, g)$ is

$$G = \frac{9\pi g^4 D^2}{4\omega_1\omega_2\omega_3\omega_4}. \tag{A4}$$

The function $D = D(\mathbf{k}_1, \mathbf{k}_2, \mathbf{k}_3, \mathbf{k}_4)$ is given by equations (B1) and (B2) of *Herterich and Hasselmann* [1980].

[85] The integration range of equation (A1) can be $\omega_1 \le \omega_2$ for symmetry with respect to $\mathbf{k}_1$ and $\mathbf{k}_2$ in equation (A1). Furthermore, integration (A1) was conducted for

$$\omega_1 \le \omega_3 \le \omega_4 \le \omega_2. \tag{A5}$$

The integration (A1) for the integration range (A5) and $\theta_{34} \le 0$ is

$$T\left(\omega_4, \theta_4^{(j_2)}\right) = \frac{\omega_4 k_4}{C_{g4}} \int_{-\pi}^{0} d\theta_{34} \int_{-\infty}^{0} d\tilde{\Omega}_{34} \int_{\theta_{ab}}^{\pi} d\theta_{a1} \\ \sum_{j_1=1}^{N_{j1}} \left(\frac{\omega_3 k_1 k_3}{C_{g1} C_{g3}} \frac{G}{S_0} N_{1234}^{(j_1,j_2)} \right) \\ = 8\omega_4^{23} g^{-10} \int_{-\pi}^{0} d\theta_{34} \int_{-\infty}^{0} d\tilde{\Omega}_{34} \int_{\theta_{ab}}^{\pi} d\theta_{a1} \\ \sum_{j_1=1}^{N_{j1}} K_b\left(\tilde{\Omega}_{34}, \theta_{a1}, \theta_{34}\right) N_{1234}^{(j_1,j_2)}, \tag{A6}$$

where

$$S_0 = \left| 1 + \frac{C_{g1}}{C_{g2}} \frac{\partial k_2}{\partial k_1} \right| = \left| 1 + \frac{C_{g1}}{C_{g2}} [k_1 - k_a \cos(\theta_{a1})] k_2^{-1} \right|, \tag{A7}$$

$$N_{1234}^{(j_1,j_2)} = \tilde{N}_1^{(j_1)} \tilde{N}_2^{(j_1)} \left(\tilde{N}_3^{(j_2)} + \tilde{N}_4^{(j_2)} \right) - \tilde{N}_3^{(j_2)} \tilde{N}_4^{(j_2)} \left(\tilde{N}_1^{(j_1)} + \tilde{N}_2^{(j_1)} \right), \tag{A8}$$

$$\tilde{N}_i^{(j)} = N\left(\omega_i, \theta_i^{(j)}\right), \\ \theta_i^{(j)} = \theta_a + (3 - 2j)\theta_{ai} \quad (i = 1, \ldots, 4,\ j = 1, 2) \tag{A9}$$

$$\theta_{ai} = \theta_i - \theta_a, \quad (i = 1, 2, 3, 4) \quad \theta_{34} = \theta_3 - \theta_4,$$

$$\tilde{\Omega}_{34} = \log(\omega_3) - \log(\omega_4), \tag{A10}$$

$$K_b\left(\tilde{\Omega}_{34}, \theta_{a1}, \theta_{34}\right) = \tilde{\omega}_1^3 \tilde{\omega}_3^4 \frac{\tilde{G}}{S_0}, \tag{A11}$$

$$\tilde{G} = \tilde{G}(\tilde{\omega}_{14}, \tilde{\omega}_{24}, \tilde{\omega}_{34}, \theta_{a1}, \theta_{a2}, \theta_{a3}, \theta_{a4}) \\ = \frac{g^4}{\omega_4^{12}} G = G(\tilde{\omega}_{14}, \tilde{\omega}_{24}, \tilde{\omega}_{34}, 1, \theta_{a1}, \theta_{a2}, \theta_{a3}, \theta_{a4}, 1), \tag{A12}$$

$\tilde{\omega}_{i4} = \omega_i/\omega_4$ (i = 1, 2, 3, 4), and k_a and θ_a are defined from $\mathbf{k}_a = (k_a \cos\theta_a, k_a \sin\theta_a)$ and equation (A3). The normalized function $\tilde{G}$ is estimated from G (equation (A4)) by replacing ω_i, k_i, θ_i and g with $\tilde{\omega}_{i4}$, $\tilde{k}_{i4} = \tilde{\omega}_{i4}^2$, θ_{ai} (i = 1, 2, 3, 4), and 1, respectively. The directions of vectors $\mathbf{k}_i$ (i = 1, 2, 3, 4) with respect to the vector $\mathbf{k}_a$ are $\theta_{a1} \ge 0$, $\theta_{a2} \le 0$, $\theta_{a3} \le 0$, and $\theta_{a4} \ge 0$, respectively. The integration range with respect to θ_{a1} in equation (A6) is

$$\theta_{ab} = \mathrm{Max}(|\theta_{a3}|, \theta_b), \tag{A13}$$

where

$$\theta_b = \arccos\left(\frac{k_a}{2k_1}\right), \quad \text{for} \quad \gamma < 0, \tag{A14}$$

$$\theta_b = 0, \quad \text{for} \quad \gamma \ge 0, \tag{A15}$$

$$\gamma = \frac{(g k_a)^{1/2}}{\omega_a} - 2^{-1/2}. \tag{A16}$$

The number of mirror images of vectors $\mathbf{k}_3$ and $\mathbf{k}_4$ ($\mathbf{k}_1$ and $\mathbf{k}_2$) with respect to vector $\mathbf{k}_a$ in quadruplets is $N_{j2} = 1$ ($N_{j1} = 1$) for $\theta_{a3} = 0$ ($\theta_{a1} = 0$) or $\omega_1 = \omega_3$. In other cases, $N_{j2} = 2$ ($N_{j1} = 2$).

[86] The integration range (A5) differs from that described by *Komatsu et al.* [1993]. The singularities at

$S_0 = 0$ ($\omega_1 = \omega_2$ and $\theta_{a1} = 0$) in equation (A6) can be avoided for (A5) [*Komatsu and Masuda*, 2001].

[87] The wave radian frequencies and directions are discretized as

$$\omega(n) = \omega_{\min} r_\omega^{n-1}, \quad (n = 1, .., N_{\max}), \tag{A17}$$

$$\theta(m) = -\pi + \frac{2\pi}{M}(m-1), \quad (m = 1, .., M), \tag{A18}$$

where $N_{\max}$ is the number of radian wave frequencies, $r_\omega = (\omega_{\max}/\omega_{\min})^{1/(N\max-1)}$ is the frequency increment, M is the number of directions, and $\omega_{\min}$ and $\omega_{\max}$ are the minimum and maximum radian frequencies, respectively. For the numerical computation, equation (A6) is discretized as

$$\begin{aligned} T\left(\omega_4, \theta_4^{(j_2)}\right) &= \sum_{m_{34}=1}^{M/2+1} \sum_{n_{34}=-N_{34}}^{0} \sum_{m_{1a}=M_{1l}}^{M} \sum_{j_1=1}^{N_{j1}} \delta T\left(\omega_4, \theta_4^{(j_2)}\right) \\ &\simeq \sum_{l_q=1}^{L_q} \sum_{j_1=1}^{N_{j1}} \delta T\left(\omega_4, \theta_4^{(j_2)}\right), \end{aligned} \tag{A19}$$

$$\delta T\left(\omega_4, \theta_4^{(j_2)}\right) = 8g^{-10}\left(\frac{2\pi}{M}\right)^2 \log(r_\omega)\omega_4^{23} K_b(\tilde{\Omega}_{34}, \theta_{a1}, \theta_{34}) N_{1234}^{(j_1, j_2)}, \tag{A20}$$

where n_3 and n_4 are the radian frequency index numbers of ω_3 and ω_4, respectively, and $\omega_3 = \omega(n_3)$, $\omega_4 = \omega(n_4)$ (equation (A17)), $n_{34} = n_3 - n_4$, and $\delta\tilde{\Omega}_{34} = (n_3 - n_4)\log(r_\omega) = n_{34}\log(r_\omega)$. The numbers m_{1a} and m_{34} are the direction index numbers of θ_{a1} and θ_{34}, respectively, and $\theta_{a1} = \theta(m_{1a})$ and $\theta_{34} = \theta(m_{34})$ (equation (A18)). $j_2 = 1, 2$ denotes mirror image quadruplets for vector $\mathbf{k}_3$ and $\mathbf{k}_4$, and $j_2 = 1$ for $\theta_{34} \le 0$ and $\theta_{a3} \le 0$. The number M_{1l} in equation (A19) is determined on the basis of equation (A13), and the number N_{34} is the parameter which determines the maximum value of ω_4/ω_3 for the numerical integration of equation (A6) as $\max(\omega_4/\omega_3) = r_\omega^{N_{34}}$. The number L_q is the total number of quadruplets for the numerical integration, and l_q is the index number of the quadruplets. The indices m_{34}, n_{34}, and m_{1a} are functions of l_q. To reduce the necessary computation, the quadruplets of $|K_b(\tilde{\Omega}_{34}, \theta_{a1}, \theta_{34})| < K_{\min}$, where $K_{\min}$ is the minimum threshold of the kernel, are excluded in the summation of the last term in equation (A19).

[88] The normalized wavenumber $\tilde{k}_{34}$ is determined from $\tilde{\Omega}_{34}$ and $\tilde{k}_{44} = 1$, and the normalized radian frequency is $\tilde{\omega}_{a4} = \tilde{k}_{34}^{1/2} + 1$ (equation (A2)). The normalized wavenumber $\tilde{k}_{a4} = k_a/k_4$ can be calculated from $\tilde{k}_{34}$, $\tilde{k}_{44} = 1$, θ_{34}, and equation (A3). The directions θ_{a3} and $\theta_{a4} = \theta_{a3} - \theta_{34}$ are calculated from $\tilde{k}_{a4}$, $\tilde{k}_{34}$ and $\tilde{k}_{44} = 1$. The normalized wavenumber $\tilde{k}_{14}$, $\tilde{k}_{24}$ and direction θ_{a2} can be calculated from equations (A2) and (A3) for a given θ_{a2}. Once we calculate the integral kernel $K_b(\tilde{\Omega}_{34}, \theta_{a1}, \theta_{34})$ (equation (A11)) for m_{34}, n_{34} and m_{1a}, we can relate m_{34}, n_{34} and m_{1a} to l_q. It is not necessary to recompute $K_b(\tilde{\Omega}_{34}, \theta_{a1}, \theta_{34})$ in each step.

[89] The wave spectral values are given on wave frequency-direction grids as equations (A17) and (A18). While (ω_4, θ_4) and (ω_3, θ_3) are on the wave frequency-direction $(\omega - \theta)$ grid points ($(\omega_4, \theta_4) = (\omega(n_4), \theta(m_4))$ and $(\omega_3, \theta_3) = (\omega(n_3), \theta(m_{34} + m_4))$), (ω_2, θ_2) and (ω_1, θ_1) are not on the wave frequency-direction grid points. The spectral values at $(\omega_i, \theta_i^{(j)})$ are evaluated by the bilinear interpolation in $\log(\omega)$ and θ using the spectral values of the wave frequency-direction $(\omega - \theta)$ grid points as

$$\begin{aligned} F\left(\omega_i, \theta_i^{(j)}\right) = \sum_{m_w=0}^{m_w=1} \sum_{n_w=0}^{n_w=1} W_s\left(m_w, n_w, \omega_i, \theta_i^{(j)}\right) F(\omega(n_i + n_w), \\ \theta\left(m_i^{(j)} + m_w\right)\Big), \end{aligned} \tag{A21}$$

where n_i and $m_i^{(j)}$ satisfy

$$\omega(n_i) \le \omega_i < \omega(n_i + 1), \quad \theta\left(m_i^{(j)}\right) \le \theta_i^{(j)} < \theta\left(m_i^{(j)} + 1\right) \tag{A22}$$

((equations (A17) and (A18)), and $W_s(m_w, n_w, \omega_i, \theta_i^{(j)})$ is the weight for the bilinear interpolation. The weight $W_s(m_w, n_w, \omega_i, \theta_i^{(j)})$ ($m_w, n_w = 0,1$) is determined from ω_i, $\theta_i^{(j)}$, and equations (A17) and (A18). The spectral values for $\omega > \omega_{\max}$ are extrapolated according to the inverse 4th power of the frequency.

[90] The integration range of equation (A6) is limited to (A5) and $-\pi \le \theta_{34} \le 0$. The integration over the full integration range (including $\omega_1 \le \omega_2$ and $-\pi \le \theta_{34} \le \pi$) is calculated as follows. In the loop of ω_4 and θ_4 (n_4 and m_4) of the numerical computation, $T_i^{(j2)}(\omega, \theta) = T(\omega_i, \theta_i^{(j2)})$ ($i = 1, 2, 3, 4$) can be updated as

$$T_i(\omega, \theta)^{(j_2)} \longrightarrow T_i^{(j_2)}(\omega, \theta) + \delta T_i^{(j_2)}(\omega, \theta), \quad (i = 1, 2, 3, 4), \tag{A23}$$

where

$$\delta T_i^{(j_2)}(\omega, \theta) = \delta T\left(\omega_i, \theta_i^{(j_2)}\right), \tag{A24}$$

$$\delta T^{(j_2)}(\omega_3, \theta_3) = \delta T\left(\omega_4, \theta_4^{(j_2)}\right), \tag{A25}$$

$$\delta T\left(\omega_1, \theta_1^{(j_2)}\right) = \delta T\left(\omega_2, \theta_2^{(j_2)}\right) = -\delta T\left(\omega_4, \theta_4^{(j_2)}\right), \tag{A26}$$

and $\delta T(\omega_4, \theta_4^{(j2)})$ is calculated from equation (A20) for $j_2 = 1, 2$. At the end of the loop of ω_4 and θ_4 (n_4 and m_4), the nonlinear source function is calculated by

$$S_{nl}(\omega, \theta) = \sum_{i=1}^{4} \sum_{j_2=1}^{N_{j2}} T_i^{(j_2)}(\omega, \theta). \tag{A27}$$

[91] However, (ω_2, θ_2) and (ω_1, θ_1) are not on the wave frequency-direction grid points. The values of $T_i^{(j2)}(\omega, \theta) = T(\omega_i, \theta_i^{(j2)})$ at four (or two) $\omega - \theta$ grid points surrounding $(\omega_i, \theta_i^{(j2)})$ are updated by adding weighted

values of $\delta T^{(j2)}(\omega_i, \theta_i)$. Equation (A23) is modified using weights in equation (A21) as

$$T_i^{(j_2)}(\omega,\theta) \longrightarrow T_i^{(j_2)}(\omega,\theta) + W_s\left(m_w, n_w, \omega_i, \theta_i^{(j_2)}\right)\delta T_i^{(j_2)}(\omega,\theta), \quad (i = 1,2,3,4) \tag{A28}$$

$$\omega = \omega(n_i + n_w), \quad \theta = \theta\left(m_i^{(j_2)} + m_w\right), \tag{A29}$$

for $\omega_{\min} \le \omega \le \omega_{\max}$, where n_i and $m_i^{(j2)}$ are determined from (A22), n_w and m_w are 0 or 1, and $\delta T_i^{(j2)}(\omega, \theta)$ is estimated from equations (A20) and (A24)–(A26). The update equation (A28) is calculated for both $j_1 = 1$ and $j_1 = 2$, if the number of mirror images of vectors $\mathbf{k}_1$ and $\mathbf{k}_2$ with respect to the vector $\mathbf{k}_a$ in quadruplets (N_{j1}) is 2.

[92] The derivatives of the nonlinear source function with respect to the wave spectrum can be calculated from equation (A24) as

$$\frac{\partial\left\{\delta T_4^{(j_2)}(\omega(n),\theta(m))\right\}}{\partial F\left(\omega(n_p),\theta(m_p)\right)} = K_c \sum_{i=1}^{4} \frac{\partial \tilde{N}_i^{(j_{12}(i))}}{\partial F\left(\omega(n_p),\theta(m_p)\right)} \frac{\partial N_{1234}^{(j_1,j_2)}}{\partial \tilde{N}_i^{(j_{12}(i))}}, \tag{A30}$$

$$\frac{\partial N_{1234}^{(j_1,j_2)}}{\partial \tilde{N}_1^{(j_1)}} = \tilde{N}_2^{(j_1)}\left(\tilde{N}_3^{(j_2)} + \tilde{N}_4^{(j_2)}\right) - \tilde{N}_3^{(j_2)}\tilde{N}_4^{(j_1)}, \tag{A31}$$

$$\frac{\partial N_{1234}^{(j_1,j_2)}}{\partial \tilde{N}_2^{(j_1)}} = \tilde{N}_1^{(j_1)}\left(\tilde{N}_3^{(j_2)} + \tilde{N}_4^{(j_2)}\right) - \tilde{N}_3^{(j_2)}\tilde{N}_4^{(j_2)}, \tag{A32}$$

$$\frac{\partial N_{1234}^{(j_1,j_2)}}{\partial \tilde{N}_3^{(j_2)}} = \tilde{N}_1^{(j_1)}\tilde{N}_2^{(j_1)} - \tilde{N}_4^{(j_2)}\left(\tilde{N}_1^{(j_1)} + \tilde{N}_2^{(j_1)}\right), \tag{A33}$$

$$\frac{\partial N_{1234}^{(j_1,j_2)}}{\partial \tilde{N}_4^{(j_2)}} = \tilde{N}_1^{(j_1)}\tilde{N}_2^{(j_1)} - \tilde{N}_3^{(j_2)}\left(\tilde{N}_1^{(j_1)} + \tilde{N}_2^{(j_1)}\right), \tag{A34}$$

$$\frac{\partial \tilde{N}_i^{(j_{12}(i))}}{\partial F\left(\omega(n_p),\theta(m_p)\right)} = \frac{g}{2\omega_i^2 k_i}\left[\sum_{m_w=0}^{m_w=1}\sum_{n_w=0}^{n_w=1} W_s\left(m_w, n_w, \omega_i, \theta_i^{(j)}\right)\delta^{n_p,m_p}_{n_i+n_w,m_i^{(j)}+m_w}\right], \tag{A35}$$

$$K_c = 8g^{-10}\left(\frac{2\pi}{M}\right)^2 \log(r_\omega)\omega_4^{23} K_b\left(\tilde{\Omega}_{34}, \theta_{a1}, \theta_{34}\right), \tag{A36}$$

where $j_{12}(i) = j_1$ for $i = 1, 2$, $j_{12}(i) = j_2$ for $i = 3, 4$, δ in equation (A35) is the Kronecker's delta defined as $\delta_{\mathbf{a}}^{\mathbf{b}} = 1$ for $\mathbf{a} = \mathbf{b}$ and $\delta_{\mathbf{a}}^{\mathbf{b}} = 0$ for $\mathbf{a} \neq \mathbf{b}$.

[93] The derivatives of the nonlinear source function with respect to the wave spectrum are calculated by updating in the same way as equation (A28) using equations (A24)–(A26) and (A30)–(A36) in the loop of ω_4 and θ_4 (n_4 and m_4). Thus the derivatives of the nonlinear source function with respect to spectral values are calculated as equation (A27).

[94] **Acknowledgments.** The author acknowledges the anonymous reviewers for their insightful comments which contributed to the improvement of the manuscript. This study was financially supported by a Grant-in-Aid for Scientific Research (C-2) from the Ministry of Education, Culture, Sports, Science, and Technology of Japan (16540403). The author acknowledges the Okinawa Radio Observatory, Communications Research Laboratory (Okinawa Subtropical Environment Remote-Sensing Center, National Institute of Information and Communications Technology) for providing Doppler spectrum data from HF ocean radar. The author acknowledges the Japan Meteorological Agency for providing the meteorological and wave data. The wave data at Nakagusuku was supplied from the Coastal Development Institute of Technology. The GFD-DENNOU Library (http://dennou.gaia.h.kyoto-u.ac.jp/arch/dcl/) was used for drawing the figures.

References

Banner, M. L., and I. R. Young (1994), Modeling spectral dissipation in the evolution of wind waves, *J. Phys. Oceanogr.*, *24*, 1550–1561.

Barrick, D. E. (1972), First-order theory and analysis of MF/HF/VHF scatter from the sea, *IEEE Trans. Antennas Propag.*, *20*, 2–10.

Donelan, M. A., J. Hamilton, and W. H. Hui (1985), Directional spectra of wind-generated waves, *Philos. Trans. R. Soc., Ser. A*, *315*, 509–562.

Georges, T. M., J. A. Harlan, L. R. Meyer, and R. G. Peer (1993), Tracking Hurricane Claudette with the U.S. Air Force over-the-horizon radar, *J. Atmos. Oceanic Technol.*, *10*, 441–451.

Hashimoto, N., L. R. Wyatt, and S. Kojima (2003), Verification of a Bayesian method for estimating directional spectra from HF radar surface backscatter, *Coastal Eng. J.*, *45*, 255–274.

Hasselmann, K. (1962), On the non-linear energy transfer in a gravity-wave spectrum. Part 1. General theory, *J. Fluid Mech.*, *12*, 481–500.

Hasselmann, S., and K. Hasselmann (1981), A symmetrical method of computing the nonlinear transfer in a gravity wave spectrum, *Hamburg Geophys. Einzelschriften, Reihe A: Wiss. Abhand. 52*, 138 pp., Univ. Hamburg, Germany.

Hasselmann, S., and K. Hasselmann (1985), Computations and parameterizations of the nonlinear energy transfer in a gravity-wave spectrum, part I: A new method for efficient computations of the exact nonlinear transfer integral, *J. Phys. Oceanogr.*, *15*, 1369–1377.

Hasselmann, D. E., M. Dunckel, and J. A. Ewing (1980), Directional wave spectra observed during JOWSWAP 1973, *J. Phys. Oceanogr.*, *10*, 1264–1280.

Hasselmann, S., K. Hasselmann, J. A. Allender, and T. P. Barnet (1985), Computations and parameterizations of the nonlinear energy transfer in a gravity wave spectrum. Part II: parameterization of the nonlinear transfer for application in wave models, *J. Phys. Oceanogr.*, *15*, 1378–1391.

Herterich, K., and K. Hasselmann (1980), A similarity relation for the nonlinear energy transfer in a finite depth gravity-wave spectrum, *J. Fluid Mech.*, *97*, 215–224.

Hisaki, Y. (1996), Nonlinear inversion of the integral equation to estimate ocean wave spectra from HF radar, *Radio Sci.*, *31*, 25–39.

Hisaki, Y. (2002), Short-wave directional properties in the vicinity of atmospheric and oceanic fronts, *J. Geophys. Res.*, *107*(C11), 3188, doi:10.1029/2001JC000912.

Hisaki, Y. (2004), Short-wave directional distribution for first-order Bragg echoes of the HF ocean radars, *J. Atmos. Oceanic Technol.*, *21*, 105–121.

Hisaki, Y. (2005), Ocean wave directional spectra estimation from an HF ocean radar with a single antenna array: Observation, *J. Geophys. Res.*, *110*, C11004, doi:10.1029/2005JC002881.

Hisaki, Y. (2006), Ocean wave directional spectra estimation from an HF ocean radar with a single antenna array: Methodology, *J. Atmos. Oceanic Technol.*, *23*, 268–286.

Hisaki, Y., and T. Naruke (2003), Horizontal variability of near-inertial oscillations associated with the passage of a typhoon, *J. Geophys. Res.*, *108*(C12), 3382, doi:10.1029/2002JC001683.

Hisaki, Y., W. Fujiie, T. Tokeshi, K. Sato, and S. Fujii (2001), Surface current variability east of Okinawa Island obtained from remotely sensed and in situ observational data, *J. Geophys. Res.*, *106*, 31,057–31,073.

Ichinari, T., and N. Kohno (1997), New numerical wave model and wave analysis and prediction system (in Japanese), *Weather Serv. Bull.*, *64*, 45–67.

Japan Meteorological Agency (1998), Geophysical review (in Japanese), *Rep. 1185*, 60 pp., Jpn. Met. Agcy., Tokyo.

Japan Meteorological Agency (1999), Annual report on ocean waves 1998 (in Japanese), report, 333 pp., Jpn. Meteorol. Agency, Tokyo.

Komatsu, K., and A. Masuda (2001), Nonlinear energy transfer among wind waves in coastal region (in Japanese), *Bull. Fish. Res. Agency*, *1*, 7–21.

Komatsu, K., T. Kusaba, and A. Masuda (1993), An efficient method for computing nonlinear energy transfer among wind waves (in Japanese), *Bull. Res. Inst. Appl. Mech. Kyushu Univ.*, *75*, 121–146.

Lipa, B. J., and B. Nyden (2005), Directional wave information from the Sea Sonde, *IEEE J. Ocean. Eng.*, *30*, 221–231.

Masuda, A. (1980), Nonlinear energy transfer between wind waves, *J. Phys. Oceanogr.*, *10*, 2082–2093.

Mitsuyasu, A., F. Tasai, T. Suhara, S. Mizuno, M. Ohkusu, T. Honda, and K. Rikiishi (1975), Observations of the directional spectrum of ocean waves using a cloverleaf buoy, *J. Phys. Oceanogr.*, *5*, 750–760.

Romeiser, R. (1993), Global validation of the wave model WAM over a one-year period using Geosat wave height data, *J. Geophys. Res.*, *98*, 4713–4726.

Shay, L. K., S. J. Lentz, H. C. Graber, and B. K. Haus (1998), Current structure variations detected by HF radar and vector measuring current meters, *J. Atmos. Oceanic Technol.*, *15*, 237–256.

Takeoka, H., Y. Tanaka, Y. Ohno, Y. Hisaki, A. Nadai, and H. Kuroiwa (1995), Observation of the Kyucho in the Bungo Channel by HF radar, *J. Oceanogr.*, *51*, 699–711.

WAMDI group (1988), The WAM model: A third generation ocean wave prediction model, *J. Phys. Oceanogr.*, *18*, 1775–1810.

Wu, J. (1980), Wind-Stress coefficients over Sea surface near neutral conditions: A revisit, *J. Phys. Oceanogr.*, *10*, 727–740.

Wyatt, L. R. (1990), A relaxation method for integral inversion applied to HF radar measurement of the ocean wave directional spectra, *Int. J. Remote Sens.*, *11*, 1481–1494.

Wyatt, L. R., L. J. Ledgard, and C. W. Anderson (1997), Maximum-likelihood estimation of the directional distribution of 0.53-Hz ocean waves, *J. Atmos. Oceanic Technol.*, *14*, 591–603.

Young, I. R., S. Hasselmann, and K. Hasselmann (1987), Computations of the response of a wave spectrum to a sudden change in wind direction, *J. Phys. Oceanogr.*, *17*, 1317–1338.

Y. Hisaki, Department of Physics and Earth Sciences, Faculty of Science, University of the Ryukyus, 1 Aza-Senbaru, Nishihara-cho, Nakagami-gun, Okinawa 903-0213, Japan. (hisaki@sci.u-ryukyu.ac.jp)